A multi-fluid model for microstructure formation in polymer membranes

Douglas R. Tree,[†] Kris T. Delaney,[†] Hector D. Ceniceros,[‡] Tatsuhiro Iwama,[¶] and Glenn H. Fredrickson[*,§]

[†]*Materials Research Laboratory, University of California, Santa Barbara, CA 93106-5121*

[‡]*Department of Mathematics, University of California, Santa Barbara, CA 93106-5121*

[¶]*Asahi Kasei Corporation, 2-1 Samejima, Fuji, Shizuoka 416-8501 Japan*

[§]*Materials Research Laboratory, Materials Department and Chemical Engineering Department, University of California, Santa Barbara, CA 93106-5121*

E-mail: drt@mrl.ucsb.edu

Abstract

We develop a multi-fluid model for a ternary polymer solution using the Rayleighian formalism of Doi and Onuki,[1] and give an efficient pseudo-spectral method for solving both the diffusion and momentum equations that result. Subsequently, we find that the numerical simulation is capable of describing systems at the micron length-scale and easily reaches millisecond time-scales. In addition, we characterize the model thermodynamics and kinetics including the (i) phase behavior, (ii) structure of the interfaces, (iii) mutual diffusion coefficients, (iv) bulk spinodal decomposition kinetics with and without hydrodynamics and (v) spinodal decomposition in the presence of an interface with a non-solvent bath. We obtain good qualitative agreement with the expected thermodynamic and kinetic behavior. We also show that a linear stability analysis of the diffusion equation quantitatively predicts the fastest growing mode

obtained from simulation and gives insight into the phase separation process relevant for the evolution of microstructure in phase-separating ternary polymer solutions.

Introduction

Immersion precipitation (IP) is a popular industrial process for fabricating polymer membranes that are used in a variety of applications, the most notable being water purification. Speaking about the IP process in 1985, McHugh and Yilmax observed that, "It is clear that a good deal of this important technology still rests on a largely empirical basis and that there is an important need for the development of quantitative models to describe the mechanisms of the structure formation process." [2] Amazingly, over thirty years later this goal has yet to be achieved. With the market size for membranes currently in the billions of dollars, and a strong expectation that the demand for clean water will increase,[3] a quantitative model of membrane formation is now more urgently needed than ever.

The canonical story of the membrane formation process by immersion precipitation is illustrated by Figure 1(a), where a mixture of polymer and good solvent is cast as a thin film onto a substrate and then immersed in a non-solvent bath.[4] Before immersion, the polymer/solvent mixture is located in the homogeneous (H) region on the schematic of the ternary phase diagram in Figure 1(b). Following immersion, solvent is exchanged for non-solvent in the polymer film, driving the mixture into the liquid-liquid coexistence region (L-L). There the film spontaneously de-mixes into a polymer-lean phase and a polymer-rich phase with some microscopic to mesoscopic inhomogeneity. Following the phase separation, the quench continues to deepen until the polymer-rich phase becomes concentrated enough to vitrify or crystallize, arresting the network structure that forms the pores of the membrane.

While this description of the origin of the membrane's microstructure is uncontroversial, it is too simple to explain the existence of various features such as "skin" layers, gradients in the pore size distribution and large-scale, finger-like pores referred to as "macro-voids".[5]

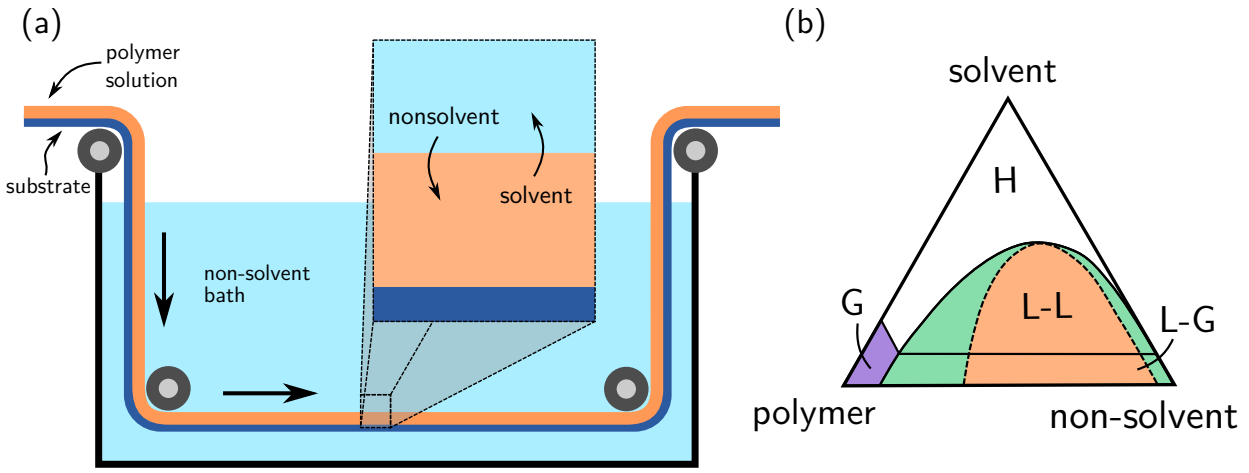

Figure 1: (a) A schematic of a roll-to-roll process for making polymer membranes by immersion precipitation. (b) A schematic ternary phase diagram with regions that are homogeneous (H), liquid-liquid coexistence (L-L), glassy (G) and liquid-glass coexistence (L-G).

As stated above, the formation mechanism of these morphological features has occupied research efforts for several decades.[4–6] Due to the lack of a fundamental explanation for the origin of these features, a number of empirical observations and heuristics have arisen surrounding the development of these morphologies, most notably surrounding macro-void formation.[7] However, beyond these empirical observations the field has made limited progress in providing a definitive qualitative explanation — let alone a quantitative model — of the mechanism of microstructure formation.

Early attempts to move beyond naked empiricism focused on calculating ternary phase diagrams[8] and developing one-dimensional transport models of solvent and non-solvent exchange.[9,10] The most useful result of these transport models are so-called "composition" or "mass-transfer" paths. Composition paths are time dependent concentration profiles plotted directly on a ternary phase diagram and are used to predict (i) the delay time between immersion and phase separation and (ii) the polymer concentration profile in the film just before demixing.

Unfortunately, one's ability to extract information about the membrane's microstructure from these models is limited, due to the fact that they do not directly treat the demixing process. Accordingly, the basic paradigm that emerged from this line of research assumed that

the microstructure would be determined by the polymer concentration profile immediately before phase separation. This in turn implied that an inhomogeneous polymer concentration would lead to an inhomogeneous membrane. Empirical observations of fast and slow delay-times before demixing were further combined with these assumptions to speculate on the mechanism of formation of various morphological features.

More recently, researchers have turned their attention to an explicit treatment of the demixing process by a wide variety of methods including phase-field,[11,12] lattice-Boltzmann,[13] dissipative particle dynamic[14] and Monte Carlo bond-fluctuation[15] models. In addition to addressing the phenomenon of non-solvent-induced phase separation (NIPS) relevant for immersion precipitation, there has also been continued interest in the related (but less complicated) process of thermally induced phase separation (TIPS).[16,17] While there are indeed many different methods used to model the demixing process, each method aims at a similar goal: to predict the kinetics of the phase transition by characterizing the rate of demixing and characteristic domain size at early times and the domain growth that results from coarsening mechanisms at late times.

Despite the existence of these models in the literature, no one has yet provided a satisfactory physical explanation of the morphological variety of polymer membranes. To put this claim in perspective, one must realize the depth of the challenge required to develop a model capable of capturing *both* mass-transfer and phase-separation kinetics. Such simulations require simultaneous and efficient treatment of spinodal decomposition kinetics, multiphase flow and multicomponent diffusion across a large span of length and time scales. Thus, while undoubtedly contributing important and unique features, each of the existing models in the literature suffers from important deficiencies (e.g. neglect of hydrodynamics, unrealistic transport coefficients, lack of non-solvent mass transfer, excessive simulation times, etc.). Furthermore, the phenomenological nature of these models detaches the connection between important parameters and macroscopic phenomena (e.g. the impact of polymer molecular weight on diffusion).

In the manuscript that follows, we develop a model rigorously connected to the statistical mechanics of polymer solutions and therefore designed to address the aforementioned deficiencies. In our approach, we use a multi-component extension of the well-known two-fluid model of de Gennes to describe the behavior of the polymer solution.[18] Following a formalism by Doi and Onuki,[1] this leads to a ternary phase-field model that we consider to be a more efficient cousin of the dynamic self-consistent field theory (SCFT) models previously used both by us and other researchers.[19–23] We then describe an accurate and efficient semi-implicit pseudo-spectral method for solving this set of non-linear PDEs, similar to those used in state-of-the-art SCFT and "model H" simulations .[24,25]

We proceed to validate the thermodynamics and kinetics of our model, and describe the length and time-scales that our simulations can access, noting that these length and time scales will allow us to describe both mass transfer and phase separation behavior in asymmetric membrane formation. We conclude with a brief investigation of the early-time spinodal decomposition kinetics and discuss the implications of these kinetics on pore-formation mechanisms in NIPS membranes. Subsequent reports will further explore the role of mass transfer in initiating spinodal decomposition and late stage coarsening kinetics as we seek to further understand the morphology selection rules of the NIPS process.

A Multi-Fluid Model

Phase-field models — like the classic Cahn-Hilliard model[26] — are an excellent choice for simulating phase-separating systems undergoing mass transfer and flow. They are capable of describing inhomogeneous systems without the need to resolve high-frequency molecular degrees of freedom that limit the time step size in particle-based methods or explicitly track interfaces like conventional multi-phase flow methods in continuum fluid dynamics. However, much of the work with phase-field models, including the Cahn-Hilliard model and model H, focuses on universal behavior.[27] Therefore, when seeking to model a specific system such

as a ternary polymer solution, one must be careful that the model accurately describes the thermodynamics and kinetics of the system of interest.

Fortunately, for polymer solutions there is a rigorous formalism connecting the statistical mechanics of polymers to field-based methods.[28] Incorporating dynamics within the field theory formalism has been a problem of interest for decades. One of the most rigorous ways to incorporate dynamics is known as the two-fluid model and was introduced by de Gennes and his colleagues in the late 1970's.[18,29] In the two-fluid model, one writes separate momentum balances for each species and then imposes a drag force between these continua to satisfy the total conservation of momentum. In addition to the drag force, one must incorporate a constitutive equation to describe the viscous and elastic stresses that the solution experiences.[20] Although technically phenomenological, such constitutive equations have deep theoretical underpinnings and a rich history in the rheology literature.[30,31]

The two-fluid model has been successful at describing important aspects of inhomogeneous polymer solutions. Indeed, it is the model of choice when accounting for the coupling between stress and concentration in such systems.[1,32,33] For example, this fact has recently been exploited by one of us (GHF and colleagues), to use a two-fluid model to postulate a unique mechanism for shear banding in polymer solutions.[34] Two-fluid models have also been important in the study of other complex fluids such as solutions of wormlike micelles.[35–37]

Doi and Onuki have developed a convenient formalism for deriving equations of motion within the two-fluid model.[1] At the heart of this formalism is a Lagrangian-type functional called a Rayleighian, which describes an over-damped (i.e., zero Reynolds-number) two-fluid model. Finding an extremum of this functional gives equations of motion that satisfy the usual principle of minimal energy dissipation in non-equilibrium thermodynamics.[38] The formalism is particularly convenient for our purposes because it naturally produces thermodynamically consistent Onsager coefficients, and it easily accommodates systems with more than two components. We note that the Doi-Onuki formalism is not the only formalism capable of producing thermodynamically consistent two-fluid models. Beris, Öttinger, Ger-

mann, Cook and others have developed a very general bracket-based Hamiltonian formalism for non-equilibrium thermodynamics that can be used for two-fluid models.[39–42]

In this section we extend the formalism of Doi and Onuki to multi-component systems to derive a "multi-fluid" model of a ternary polymer solution. Our model includes thermodynamically consistent, concentration-dependent diffusivities and hydrodynamics, key features for correctly describing the NIPS process that were lacking in previous phase-field models.[11,12] In its current incarnation, our model does not include elastic stresses, which are certain to play an important role during the solidification of the membrane at high polymer concentration. Thermal fluctuations are also neglected, which would permit the system to overcome barriers to metastability. Omitting these physical effects allows us to greatly simplify the numerical methods while providing an opportunity to tease out the impact of diffusion and viscosity alone. However, these effects are experimental realities and research regarding their inclusion is ongoing.

In the next section, we build a Rayleighian that includes the physical effects we just described, and present the corresponding transport equations. The Supplemental Information provides additional details about the derivation of the transport equations. Following the derivation, we present efficient numerical methods for solving the transport equations, which are a set of coupled, non-linear partial differential equations.

Model description

Consider a ternary mixture of a polymer (p), non-solvent (n) and good solvent (s) where each component is characterized by a scalar density field, $\rho_i(\boldsymbol{r})$, and a vector-valued velocity field, $\boldsymbol{v}_i(\boldsymbol{r})$, with $i \in \{p, n, s\}$. Unfortunately, the co-existence of multiple spatial dimensions and multiple species represents a notational challenge. To avoid ambiguity, we represent vectors and tensors in spatial dimensions using bold variables (e.g. $\boldsymbol{v}$) and use explicit subscripts for species variables (e.g. H_{ij}).

To derive transport equations for these components using the Doi-Onuki formalism, we

need (i) an expression of the principle of conservation of mass and (ii) a Rayleighian functional.[1,38] Accordingly, each component in the system satisfies a mass-conservation relationship

$$\frac{\partial \rho_i}{\partial t} = -\nabla \cdot (\rho_i \boldsymbol{v}_i)\,. \tag{1}$$

With an eye towards using the Flory–Huggins model for thermodynamic properties, we assume that each component has the same partial molar volume, $\tilde{\mathrm{v}}_i = \mathrm{v}_0$ (i.e., monomer size, $b = \mathrm{v}_0^{1/3}$), where v_0 is a constant. With this assumption, $\rho_i = \phi_i \mathrm{v}_0^{-1}$, and Eq. 1 simplifies to,

$$\frac{\partial \phi_i}{\partial t} = -\nabla \cdot (\phi_i \boldsymbol{v}_i) \tag{2}$$

where $\phi_i(\boldsymbol{r})$ is the volume fraction of component i.

Assuming $\tilde{\mathrm{v}}_i = \mathrm{v}_0$ may seem restrictive, especially since Tsay and McHugh argued that the ratio of molar volumes was an important parameter for modeling the relative flux of solvent to non-solvent in their 1D mass-transfer model.[10] However, the assumption is not as limiting as it appears. In fact, we retain the freedom to assume different molecular sizes (and therefore different relative fluxes) through the use of a parameter for the degree of polymerization. The real consequence of the assumption of constant partial molar volume is on the total density. Under this assumption, the total density is a constant, $\rho = \mathrm{v}_0^{-1}$, meaning the mixture is incompressible

$$\nabla \cdot \boldsymbol{v} = 0 \tag{3}$$

where we have introduced the total (barycentric) solution velocity

$$\boldsymbol{v} = \sum_{i}^{p,n,s} \phi_i \boldsymbol{v}_i. \tag{4}$$

Note that with incompressibility, we lose a degree of freedom in specifying one concentration field. In other words, when Eq. 3 is satisfied in our three-fluid case, the number of inde-

pendent component mass balances (i.e., Eq. 2) decreases from three to two. When taking derivatives or evaluating material constants, it will prove convenient to use only the independent volume fractions. Therefore, we adopt a convention where only the polymer and the non-solvent volume fractions are independent variables and the solvent volume fraction is given by,

$$\phi_s = 1 - \sum_i^{p,n} \phi_i. \tag{5}$$

The Rayleighian

The Rayleighian is a functional of the component velocity fields and is a Lagrangian-type expression for dissipative processes composed of three terms:

$$R[\{\boldsymbol{v}_i\}] = \dot{F}[\{\boldsymbol{v}_i\}] + \Phi[\{\boldsymbol{v}_i\}] - \lambda G[\{\boldsymbol{v}_i\}] \tag{6}$$

the time derivative of the Helmholtz free energy of mixing, $\dot{F}[\{\boldsymbol{v}_i\}]$, the dissipation potential, $\Phi[\{\boldsymbol{v}_i\}]$, and a Lagrangian constraint, $G[\{\boldsymbol{v}_i\}]$, with multiplier, λ.[1,38,43]

The free energy functional is given by a generalization of the Flory–Huggins–de Gennes functional for a ternary system (noting the two independent variables ϕ_p and ϕ_n),[29]

$$F[\{\phi_i\}] = \frac{k_B T}{\mathrm{v}_0} \int d\boldsymbol{r} \left[f_0(\{\phi_i\}) + \frac{1}{2} \sum_i^{p,n} \kappa_i \left| \nabla \phi_i \right|^2 \right] \tag{7}$$

$$f_0(\{\phi_i\}) = \sum_i^{p,n,s} \frac{\phi_i}{N_i} \ln \phi_i + \sum_{i \neq j}^{p,n,s} \chi_{ij} \phi_i \phi_j \tag{8}$$

where k_B is Boltzmann's constant, T is the absolute temperature and v_0 is the reference volume. $f_0(\{\phi_i\})$ is the homogeneous free energy of mixing given by a ternary Flory–Huggins model, where N_i parameterizes the degree of polymerization, and χ_{ij} are Flory interaction parameters. The non-local terms in Eq. 7 are preceded by gradient coefficients, κ_i. In principle, one can derive composition-dependent gradient coefficients using a microscopic polymer model and an analytical approximation such as the random phase approximation

or a slow gradient expansion.[28,29,44] However, we leave them as constants to simplify both the model and numerical methods.

The Rayleighian requires the time derivative of the free energy functional. Taking the derivative and using the chain rule gives

$$\dot{F}[\{\boldsymbol{v}_i\}] = \int d\boldsymbol{r} \left[\sum_i^{p,n} \frac{\delta F}{\delta \phi_i} \frac{\partial \phi_i}{\partial t} \right]. \tag{9}$$

Using the mass balance expression in Eq. 2 for the time derivative of the volume fraction, defining the (exchange) chemical potential

$$\mu_i = \frac{\delta F}{\delta \phi_i} \tag{10}$$

and using integration by parts gives

$$\dot{F}[\{\boldsymbol{v}_i\}] = \int d\boldsymbol{r} \left[\sum_i^{p,n} \phi_i \boldsymbol{v}_i \cdot \nabla \mu_i \right] \tag{11}$$

which expresses the time derivative of the free energy in terms of the component velocities.

The dissipation potential represents one half of the rate of energy dissipation of the fluid and is given by

$$\Phi[\{\boldsymbol{v}_i\}] = \frac{1}{2} \int d\boldsymbol{r} \left[\sum_i^{p,n,s} \zeta_i \left(\boldsymbol{v}_i - \boldsymbol{v}_m \right)^2 + \boldsymbol{\sigma}^{(\mathrm{v})} : \nabla \boldsymbol{v} \right]. \tag{12}$$

The dissipation potential includes a sum over the drag between components and a viscous dissipation term. The viscous stress tensor is assumed to be quasi-Newtonian,

$$\boldsymbol{\sigma}^{(\mathrm{v})} = \eta(\{\phi_i\})[\nabla \boldsymbol{v} + (\nabla \boldsymbol{v})^{\mathrm{T}}] \tag{13}$$

where $\eta(\{\phi_i\})$ is a concentration-dependent solution viscosity to be specified. While the concentration-dependent viscosity in Eq. 13 does not include the full effects of viscoelasticity that would accompany an elastic free energy contribution in Eq. 7 and a stress relaxation

term in Eq. 12, it does give the model the freedom to produce dynamics with some features that resemble a glassy solid by allowing the viscosity to become large at a high polymer concentration. The drag in Eq. 12 is defined relative to the friction-centered "medium velocity",[1]

$$\boldsymbol{v}_m = \frac{1}{\zeta}\sum_i^{p,n,s} \zeta_i \boldsymbol{v}_i \tag{14}$$

where ζ_i is the friction per volume of component i, and $\zeta = \sum_i \zeta_i$ is the total friction density. Doi and Onuki have shown that it is necessary to use the medium velocity in the drag term in order to get correct mutual diffusion coefficients.[1]

The friction coefficients, ζ_i, are assumed to be local and embody the low-frequency details of polymer-solvent dynamics.[23,45] In our model, we follow Doi and Onuki,[1] and assume that the viscous stresses are the only non-local dissipative terms. We further assume that the friction coefficient density is proportional to the monomer friction coefficient times the component density (i.e., the friction is Rouse-like),

$$\zeta_i = \mathrm{v}_0^{-1}\zeta_0\phi_i \tag{15}$$

where the friction coefficient of a monomer of size b is defined as,

$$\zeta_0 = \eta_s b \tag{16}$$

which is the Stokes friction in a dilute solution where the usual factor of 6π is omitted for arithmetic convenience. Notice that the degree of polymerization, N_i, does not enter into Eq. 15 because ζ_i is a friction per volume, not a friction per molecule.

Finally, the incompressibility constraint on species velocity fields must also be accounted for in the Rayleighian,

$$\lambda G[\{\boldsymbol{v}_i\}] = \int d\boldsymbol{r}\, p\,(\nabla\cdot\boldsymbol{v}) \tag{17}$$

where the Lagrange multiplier is defined as the pressure, p. Note that the incompressibility

constraint on masses has been satisfied by construction in the free energy functional.

Model Summary

Substituting Equations 11, 12 and 17 into Eq. 6 fully specifies the Rayleighian. Stationary values of the Rayleighian with respect to $\boldsymbol{v}_i$ yield equations of motion for the component velocities. Subsequent re-arrangements of the component velocity equations, which are detailed in the Supplemental Information, yield a coupled set of momentum and diffusion equations. The resulting transport equations are non-dimensionalized by the length scale $R = bN_r^{1/2}$ (the RMS end-to-end distance of a reference polymer of length N_r), the time scale $\tau = N_r^2 \eta_r \mathrm{v}_0 / k_B T$ (the Rouse time of the reference polymer in a solution with viscosity η_r), and the viscous pressure scale $p^* = \eta_r / \tau$.

The final result of this process is the set of dimensionless transport equations:

$$\frac{\partial \phi_i}{\partial t} + \boldsymbol{v} \cdot \nabla \phi_i = \nabla \cdot \left[\sum_j^{p,n} M_{ij} \nabla \mu_j \right] \tag{18}$$

$$-\nabla p + \nabla \cdot \left[\eta(\{\phi_i\}) (\nabla \boldsymbol{v} + \nabla \boldsymbol{v}^T) \right] = N_r \sum_i^{p,n} \phi_i \nabla \mu_i \tag{19}$$

$$\nabla \cdot \boldsymbol{v} = 0 \tag{20}$$

$$\nabla \mu_i = \sum_j^{p,n} \Big[H_{ij} \nabla \phi_j - K_{ij} \nabla \nabla^2 \phi_j \Big]. \tag{21}$$

The transport equations include two convection-diffusion equations (Eq. 18), a total momentum balance (Eq. 19), the incompressibility constraint (Eq. 20) and the gradient of the chemical potential (Eq. 21). Additionally, the matrix of mobility (Onsager) coefficients is given by,

$$M_{pp} = \phi_p (1 - \phi_p) \tag{22a}$$

$$M_{pn} = M_{np} = -\phi_p \phi_n \tag{22b}$$

$$M_{nn} = \phi_n (1 - \phi_n) \tag{22c}$$

Table 1: Dimensionless Parameters

Expression	Description
$\alpha_p = N_p/N_r$	polymer size
$\alpha_n = N_n/N_r$	non-solvent size
$\alpha_s = N_s/N_r$	solvent size
$\chi_{ps}N_r$	polymer-solvent interaction
$\chi_{ns}N_r$	non-solvent-solvent interaction
$\chi_{pns}N_r = (\chi_{pn} - \chi_{ns} - \chi_{ps})N_r$	solvent-mediated polymer-non-solvent interaction
$\tilde{\kappa}_p = \kappa_p b^{-2}$	polymer-solvent gradient coefficient
$\tilde{\kappa}_n = \kappa_n b^{-2}$	non-solvent-solvent gradient coefficient

the Hessian matrix of the second derivatives of the homogeneous free energy functional is,

$$H_{pp} = (\alpha_p \phi_p)^{-1} + (\alpha_s \phi_s)^{-1} - 2\chi_{ps}N_r \tag{23a}$$

$$H_{pn} = H_{np} = (\alpha_s \phi_s)^{-1} + \chi_{pns}N_r \tag{23b}$$

$$H_{nn} = (\alpha_n \phi_n)^{-1} + (\alpha_s \phi_s)^{-1} - 2\chi_{ns}N_r \tag{23c}$$

and the matrix of the gradient coefficients is given by

$$K_{pp} = \kappa_p \tag{24a}$$

$$K_{pn} = K_{np} = 0 \tag{24b}$$

$$K_{nn} = \kappa_n. \tag{24c}$$

A summary of the dimensionless parameters which appear in Equations 18–21 is provided in Table 1. (Note that all parameters are physically constrained to be positive, real numbers.) For typographical clarity, tildes have been omitted on the dimensionless variables in Equations 18–24.

Numerical Methods

The multi-fluid model expressed in Equations 18–24 is a set coupled non-linear partial differential equations. There are a number of challenges to obtaining an accurate and efficient

numerical solution. It can be shown that the fourth-order spatial derivatives in Eq. 18 cause numerical instabilities in explicit time-stepping schemes unless

$$\Delta t < c\,(\Delta x)^4 \tag{25}$$

where Δt is the time step, Δx is the grid resolution and c is some constant that depends on the physical constants and the specifics of the method.[24] Since $\Delta x \ll 1$ is required for accurately resolving interfaces, Eq. 25 is an oppressive limitation, and an implicit scheme is necessary. However, fully implicit methods can be costly and difficult to implement. Instead, we employ a cost efficient semi-implicit alternative.

In addition to the notorious numerical stiffness problem, solutions with phase-separated domains contain narrow interfaces, which introduce small length scales that must be resolved. These interfaces are dynamic, so using lower-order finite difference methods requires highly-resolved grids, which limit system size and can become prohibitively expensive. As such, one desires a high-accuracy method that converges rapidly with mesh size to the fully resolved limit.

More computational challenges are presented by the momentum equation, Eq. 19. Like all methods for incompressible fluids, one must find an efficient way to enforce the incompressibility constraint through the pressure term. The concentration-dependent viscosity in Eq. 19 adds an additional complication. As is the case with the diffusion equation, the hope is to resolve this issue without having to break linear scaling by resorting to costly non-linear solvers (e.g. Newton's method).

We have developed a linearly implicit, pseudo-spectral method designed to address these challenges. For the time discretization, we use a semi-implicit scheme, which has been shown to be a stable and efficient method for overcoming the difficulties associated with high-order derivatives in model H.[24,25,46] The spatial derivatives are treated with pseudo-spectral methods. The accuracy of spectral methods is unparalleled, making them the method of choice

for resolving domain interfaces in related problems such as self-consistent field theory.[25,28] Pseudo-spectral methods also simplify the treatment of the incompressibility constraint in the momentum equation, through the use of a closed-form projection operator.[30,47]

Finally, until now we have neglected to discuss boundary conditions and simulation geometry. The choice of numerical method is often constrained by both considerations. For the purposes of this paper, we assume periodic boundary conditions and a rectangular geometry. Periodic boundary conditions and rectangular geometries are readily implemented with pseudo-spectral methods[48–51] and are not limiting for our current tasks of characterizing the model and investigating homogeneous spinodal decomposition kinetics. The accommodation of additional boundary conditions is the focus of ongoing work.

The diffusion equation

Consider Eq. 18

$$\frac{\partial \phi_i}{\partial t} + \boldsymbol{v} \cdot \nabla \phi_i = \nabla \cdot \left[\sum_j \left(D_{ij} \nabla \phi_j - B_{ij} \nabla \nabla^2 \phi_j \right) \right] \tag{26}$$

where we define the Fickian diffusion matrix as,

$$D_{ij} = \sum_k M_{ik} H_{kj} \tag{27}$$

and the product of the mobility and gradient coefficient matrices as,

$$B_{ij} = \sum_k M_{ik} K_{kj}. \tag{28}$$

In general, the coefficient matrices D_{ij} and B_{ij} depend on concentration and therefore are functions of space. However, consider for a moment the case where they are constants. Taking the spatial Fourier transform of both sides gives,

$$\frac{\partial \hat{\phi}_i}{\partial t} + \mathcal{F}[\boldsymbol{v} \cdot \nabla \phi_i] = -\sum_j \left(q^2 D_{ij} + q^4 B_{ij} \right) \hat{\phi}_j \tag{29}$$

where we represent the Fourier transform of a function as,

$$\mathcal{F}[\phi_i(\boldsymbol{r})] = \int d\boldsymbol{r}\, \phi(\boldsymbol{r}) \exp(-i\boldsymbol{q}\cdot\boldsymbol{r}) \tag{30}$$

$$= \hat{\phi}(\boldsymbol{q}) \tag{31}$$

and $q^2 = |\boldsymbol{q}|^2$ and $q^4 = |\boldsymbol{q}|^4$. Using a first-order finite difference approximation for the time-derivative, we treat the gradient terms implicitly and the convection term explicitly,

$$\frac{\hat{\phi}_i^{(n+1)} - \hat{\phi}_i^{(n)}}{\Delta t} + \mathcal{F}[\boldsymbol{v}^{(n)}\cdot\nabla\phi_i^{(n)}] = -\sum_j \left(q^2 D_{ij} + q^4 B_{ij}\right)\hat{\phi}_j^{(n+1)} \tag{32}$$

where superscripts are used to denote the time index. Re-arranging and solving for $\phi_i^{(n+1)}$ gives,

$$\hat{\phi}_j^{(n+1)} = \sum_i (A^{-1})_{ji}\left(\hat{\phi}_i^{(n)} - \Delta t\, \mathcal{F}[\boldsymbol{v}^{(n)}\cdot\nabla\phi_i^{(n)}]\right) \tag{33}$$

where we have defined,

$$A_{ij} \equiv I_{ij} + \Delta t\, q^2 D_{ij} + \Delta t\, q^4 B_{ij}. \tag{34}$$

I_{ij} is the identity matrix (in components p and n) and $(A^{-1})_{ji}$ represents the inverse of A_{ij}, which in this case is a 2×2 matrix for the two independent species.

We expect the method given in Eq. 33 to overcome the stability limit of Eq. 25 because it is implicit in the second and fourth order gradients. Additionally, assuming we discretize space with $\mathcal{M}$ plane waves, numerically evaluating Eq. 33 takes only $\mathrm{O}(\mathcal{M}\log\mathcal{M})$ operations. This computational cost is nearly optimal. (We must also invert a 2×2 matrix to uncouple the interdependence of the different species, but this is trivial.) Because we have treated the convection term explicitly, we are still limited by the so-called CFL stability limit. However, the CFL limit is not nearly as restrictive as Eq. 25, and we do not expect it to drastically affect the performance of the method.[24]

Incorporating these insights when D_{ij} and B_{ij} are variable, we use a splitting approach

in which we extract constant coefficient linear terms which are dominant at small scales. Let

$$d_{ij} = \max(D_{ij}) \tag{35}$$

$$b_{ij} = \max(B_{ij}) \tag{36}$$

where max() returns the matrix at the spatial grid point with the largest eigenvalue (either globally or at each time step). This can be conveniently done by searching space for the matrix with the largest norm. Then we add and subtract the leading order terms with constant coefficients d_{ij} and b_{ij} to Eq. 26,

$$\frac{\partial \phi_i}{\partial t} + \boldsymbol{v} \cdot \nabla \phi_i = \sum_j \left[d_{ij} \nabla^2 \phi_j - b_{ij} \nabla^4 \phi_j + \nabla \cdot (\delta D_{ij} \nabla \phi_j) - \nabla \cdot \left(\delta B_{ij} \nabla \nabla^2 \phi_j \right) \right] \tag{37}$$

where $\delta D_{ij} = D_{ij} - d_{ij}$ and $\delta B_{ij} = B_{ij} - b_{ij}$. Taking the Fourier transform and discretizing as before gives,

$$\begin{aligned} \frac{\hat{\phi}_i^{(n+1)} - \hat{\phi}_i^{(n)}}{\Delta t} + \mathcal{F}[\boldsymbol{v}^{(n)} \cdot \nabla \phi_i^{(n)}] = \sum_j \Bigg\{ & - \left(d_{ij} q^2 + b_{ij} q^4 \right) \hat{\phi}_j^{(n+1)} \\ & + \mathcal{F}\left[\nabla \cdot \left(\delta D_{ij}^{(n)} \nabla \phi_j^{(n)} \right) \right] - \mathcal{F}\left[\nabla \cdot \left(\delta B_{ij}^{(n)} \nabla \nabla^2 \phi_j^{(n)} \right) \right] \Bigg\} \end{aligned} \tag{38}$$

where we have treated the linearized stiffest terms implicitly and the rest explicitly. Re-arranging to solve for $\phi_i^{(n+1)}$ gives,

$$\begin{aligned} \hat{\phi}_j^{(n+1)} = \sum_i \left(A^{-1} \right)_{ji} \Bigg\{ & \hat{\phi}_i^{(n)} - \Delta t \mathcal{F}\left[\boldsymbol{v}^{(n)} \cdot \nabla \phi_i^{(n)} \right] \\ & + \Delta t \mathcal{F}\left[\nabla \cdot \left(\delta D_{ij}^{(n)} \nabla \phi_j^{(n)} \right) \right] - \Delta t \mathcal{F}\left[\nabla \cdot \left(\delta B_{ij}^{(n)} \nabla \nabla^2 \phi_j^{(n)} \right) \right] \Bigg\}. \end{aligned} \tag{39}$$

The linearly implicit approach outlined here improves stability as long as D_{ij} and B_{ij} are positive definite. The underlying diffusion equation is not stable when this condition is not satisfied (e.g. D_{ij} is not positive definite when inside the spinodal region). Therefore

any implementation of this procedure should carefully check that d_{ij} and b_{ij} are positive definite. To ensure maximum numerical stability in our implementation, we perform a spectral decomposition of d_{ij} and b_{ij} at each time step. If a negative eigenvalue is found, the matrix d_{ij} or b_{ij} is re-constructed, with unstable modes eliminated resulting in a sub-space semi-implicit method.

Momentum Equation

Now consider Eq. 19,

$$-\nabla p + \nabla \cdot \left[\eta(\nabla \boldsymbol{v} + \nabla \boldsymbol{v}^T)\right] = N_r \nabla \cdot \boldsymbol{\Pi} \tag{40}$$

where we have re-written the right-hand side in terms of the osmotic stress tensor,[1,33,47,52]

$$\nabla \cdot \boldsymbol{\Pi} = \sum_{i}^{n,p} \phi_i \nabla \mu_i. \tag{41}$$

As was the case with the diffusion equation, our numerical method is easiest to illustrate with constant coefficients, so for the moment we assume that the viscosity is a constant. Simplifying Eq. 40 gives

$$-\nabla p + \eta \nabla^2 \boldsymbol{v} = N_r \nabla \cdot \boldsymbol{\Pi}. \tag{42}$$

The main challenge to overcome in solving Eq. 42 is enforcing incompressibility and thereby eliminating ∇p. One effective way to do this when using pseudo-spectral methods is the direct application of the transverse projection operator, $\boldsymbol{T}$.[52] The transverse projection operator has the useful property that it projects out a divergence-free velocity field

$$\hat{\boldsymbol{T}} \cdot \hat{\boldsymbol{v}} = \hat{\boldsymbol{v}} \tag{43}$$

$$\hat{\boldsymbol{T}} \cdot \widehat{\nabla p} = 0 \tag{44}$$

and it can be represented explicitly in Fourier space

$$\hat{\boldsymbol{T}} = \boldsymbol{I} - \frac{\boldsymbol{qq}}{q^2}. \tag{45}$$

Using these properties, we take the Fourier transform of Eq. 42, apply $\boldsymbol{T}$ to both sides and solve for $\hat{\boldsymbol{v}}$,

$$\hat{\boldsymbol{v}}^{(n+1)} = -\frac{1}{\eta q^2}\left[\boldsymbol{I} - \frac{\boldsymbol{qq}}{q^2}\right] \cdot \mathcal{F}\left[N_r \nabla \cdot \boldsymbol{\Pi}^{(n+1)}\right] \tag{46}$$

where we labeled the time step with the same notation as used in the diffusion equation, Eq. 39. The solution is accurate and efficient, requires no iteration, and can be directly calculated following the evaluation of Eq. 39. Notice that the velocity is slaved to the osmotic stress forcing term. This is a consequence of the lack of inertia in Stokes' flow.

Using the constant viscosity problem as a guide, we now address the variable viscosity case. Analogous to the semi-implicit method for the diffusion equation, we add and subtract a viscous dissipation term with a constant viscosity

$$\eta^* = \max(\eta) \tag{47}$$

to the variable viscosity momentum equation,

$$-\nabla p + \eta^* \nabla^2 \boldsymbol{v} + \nabla \cdot \left[\delta\eta(\nabla \boldsymbol{v} + \nabla \boldsymbol{v}^T)\right] = N_r \nabla \cdot \boldsymbol{\Pi} \tag{48}$$

where we have defined $\delta\eta \equiv \eta - \eta^*$. Taking the Fourier transform and applying the transverse projection operator to both sides yields,

$$\hat{\boldsymbol{v}} = -\frac{1}{\eta^* q^2}\left[\boldsymbol{I} - \frac{\boldsymbol{qq}}{q^2}\right] \cdot \mathcal{F}\left[N_r \nabla \cdot \boldsymbol{\Pi} - \nabla \cdot \left[\delta\eta(\nabla \boldsymbol{v} + \nabla \boldsymbol{v}^T)\right]\right] \tag{49}$$

which is an implicit equation for $\hat{\boldsymbol{v}}$. We can solve for $\hat{\boldsymbol{v}}$ by treating the velocity on the right-

and left-hand sides of the equation as being at different fictitious time steps m,

$$\hat{\boldsymbol{v}}^{(m+1)} = -\frac{1}{\eta^* q^2}\left[\boldsymbol{I} - \frac{\boldsymbol{q}\boldsymbol{q}}{q^2}\right] \cdot \mathcal{F}\left[N_r \nabla \cdot \boldsymbol{\Pi}^{(n+1)} - \nabla \cdot \left[\delta\eta(\nabla \boldsymbol{v}^{(m)} + (\nabla \boldsymbol{v}^{(m)})^T)\right]\right]. \tag{50}$$

Eq. 50 can be solved by a fixed-point method, which is iterated in an inner loop during each time step until $\left|\boldsymbol{v}^{(m+1)} - \boldsymbol{v}^{(m)}\right| \leq \epsilon$ where ϵ is some tolerance. At this point $\hat{\boldsymbol{v}}^{(m+1)} \to \hat{\boldsymbol{v}}^{(n+1)}$ and time-stepping continues. In our experience, the fixed-point method is stable when $\eta^* = \max(\eta)$, however, convergence can take many steps when the viscosity ratio, $\max(\eta)/\min(\eta)$, is large. Such iterations are very costly, since the fixed-point iteration occurs as an inner loop at each time step. To decrease these costs, we implemented (i) a first-order continuation method between time steps n and $n+1$ to obtain better guesses of the initial value of the velocity fields and (ii) Anderson mixing to accelerate the convergence of the fixed-point method.[53,54] Additionally, we exploit the fact that the osmotic stress term in Eq. 50 does not change in the inner loop, and therefore its contribution to the velocity only needs to be computed once.

Implementation

We have implemented these methods in a custom CUDA/C++ code for general-computing graphics processing units (GPGPUs), which are very efficient at performing the Fourier transforms required by the pseudo-spectral method.[55]

On a single GPU, simulation size is typically limited by memory, rather than processor time. Using a Tesla M2070 with 6 GB global memory we have run jobs with as many as $1024^2 \approx 10^6$ plane waves. A typical spatial resolution is $0.5R$ (depending on the interface thickness), meaning in a typical two-dimensional simulation, we have an maximum simulation domain size of approximately $512R \times 512R$. For a typical polymer size of 100 Å, this translates to a simulation domain of about $5\,\mu\text{m} \times 5\,\mu\text{m}$.

Additionally, we have implemented an adaptive time-stepping scheme to leverage the

improved stability imparted by the semi-implicit method to allow for larger time steps, when doing so does not incur an accuracy penalty. For a given degree of time step accuracy, the optimal step size depends on details of the current-time dynamics. Using a constant time step scheme clearly limits one to the worst-case time step, thereby limiting the total simulation time achievable for a given wall-clock time. Accordingly, we use a step-doubling procedure that controls the truncation error, $\epsilon = |\left(\phi_i^{n+1}\right)_{\Delta t} - \left(\phi_i^{n+1}\right)_{\Delta t/2}|$, of the diffusion equation to within $\epsilon \leq [10^{-4}, 10^{-6}]$.[56] The use of the adaptive time-stepper accurately treats fast dynamics with smaller time steps, while permitting numerical acceleration during more inert periods, thereby enabling a significant decrease to the wall-clock time needed to reach large time-scales.

Because of the step-doubling procedure and the iterative nature of the momentum equation, the wall-clock times necessary to reach a specific simulation can vary widely based on the parameters of the model and initial conditions. A less variable parameter is the wall-clock time per time step, which for the spinodal decomposition studies that follow were typically about 0.33 seconds on a single Tesla M2070 GPU. To give a sense of the accessible time-scales, we note that while performing the simulations for Figure 6, we were able to reach simulation times of 6×10^4 in approximately 2×10^5 time steps in 10–20 hours wall-time. Converting simulation time to dimensional units assuming $N_r = 20$, $b = 10$ Å, $\eta_r = 1$ cP and $T = 293K$ gives $\tau \approx 0.1$ μs and therefore a time of ≈ 6 ms for these spinodal decomposition simulations.

Finally, we mention the effect of several key parameters on the overall stability and efficiency of the numerical method. High segregation strength simulations (i.e., $\chi_{ps}N_p \gtrsim 30$) are a particular challenge. Here, the equilibrium volume fraction of a component is often very close to zero or one, due to the presence of the logarithmic terms in the Flory–Huggins free energy, Eq. 8. Numerical accuracy becomes limiting in these situations and the numerical method becomes unstable. In addition, interfaces narrow at high segregation strength, and spectral derivatives become less accurate as they populate modes with increasingly higher

wave number. To solve this problem, one may increase the grid resolution, or widen the interfaces by increasing the value of κ_i. (Although the latter solution is mathematically possible, the values κ_i are often constrained by physical considerations.)

Simulations with a large viscosity contrast (η_p/η_s) also present a challenge. As expected, errors converge linearly using the naive fixed-point method, which can take dozens or hundreds of iterations when the viscosity contrast is order ten or greater. Using better initial guesses with a continuation method and accelerating convergence by using Anderson mixing, we were able to make up to a ten-fold decrease in the number of iterations in the inner loop over the naive implementation, depending on the viscosity contrast. With these improvements, calculations with a viscosity contrast up to at least 10^4 are achievable within roughly the same order of magnitude of wall-clock time as a constant viscosity calculation.

Results and Discussion

Thermodynamics

To validate our model, we start by examining equilibrium behavior. The behavior of the phase-field model at equilibrium is governed by the ternary Flory-Huggins-de Gennes (FHG) functional given in Eq. 7. Flory-Huggins based phase-field models are very well understood, and have a number of limitations when comparing to experimental systems. They are mean-field models,[57] and the interaction parameters (i.e., χ_{ij}) must be given a dependence on temperature, concentration and sometimes molecular weight to obtain agreement with experiments.[58,59] As such, a number of studies of polymer membrane formation in the literature have used concentration-dependent interaction parameters.[8,60,61] While these changes do indeed produce quantitatively different phase diagrams, we hypothesize that existence of concentration-dependent χ-parameters will only subtly impact the qualitative dynamic behavior, meaning that we can focus our attention on constant χ_{ij} parameters. If this hypothesis is invalid or if quantitative agreement is necessary for a particular application, the

free-energy functional and its derivatives can be modified accordingly.

With arbitrary species' molecular weight and interaction parameters, the FHG functional is general enough to produce multi-phase systems well beyond the scope of the two-phase NIPS problems that concern us here. Therefore, we restrict our attention to two-phase polymer solutions, where the only phase separation is between the polymer and non-solvent. This regime of the parameter space is characterized by a polymer molecular weight much larger than that of the solvent and non-solvent ($\alpha_p \gg \alpha_s,\ \alpha_n$) and interaction parameters χ_{ns} and χ_{ps} below their critical values. For characterization purposes, we define a pseudo-binary system that satisfies these criteria: (i) $\alpha_p = 1$, (ii) $\alpha_n = \alpha_s = N^{-1}$, (iii) $N_r = N$, (iv) $\chi = \chi_{pn}$, (v) $\chi_{ps} = \chi_{ns} = 0$, and (vi) $\kappa = \kappa_p = \kappa_n$. With these assumptions we have only three degrees of freedom (N, χ and κ) in addition to the composition variables ϕ_p and ϕ_n.

Within this parameter space, we first verify that the multi-fluid model produces the expected phase behavior. Figure 2 compares phase-separated states obtained from the multi-fluid model to a ternary phase diagram generated from the homogeneous free energy in Eq. 8. Panels (a)–(c) shows spatial profiles of the polymer density for half of the simulation domain; symmetry renders the other half of the periodic box redundant. The density profiles are equilibrium profiles, obtained by running the multi-fluid simulation in two stages. The first stage uses an initial condition consisting of a homogeneous profile at the average concentration (inside the spinodal) with a small sinusoidal perturbation. This stage undergoes spinodal decomposition and yields many domains, with compositions that differ from equilibrium due to the finite size of the domains. To avoid the need to resolve the long (i.e., logarithmic[62]) time-scale of 1D coarsening dynamics of these domains, these simulations are stopped and used to initialize a second stage of calculations with only two domains separated by a sigmoidal interface of width $\approx R$ at the near-equilibrium concentration. These calculations are run until the density profiles equilibrate.

Figure 2(d) shows each collocation point of the density profiles in composition space along with the ternary phase diagram. The phase diagram consists of a critical point, a

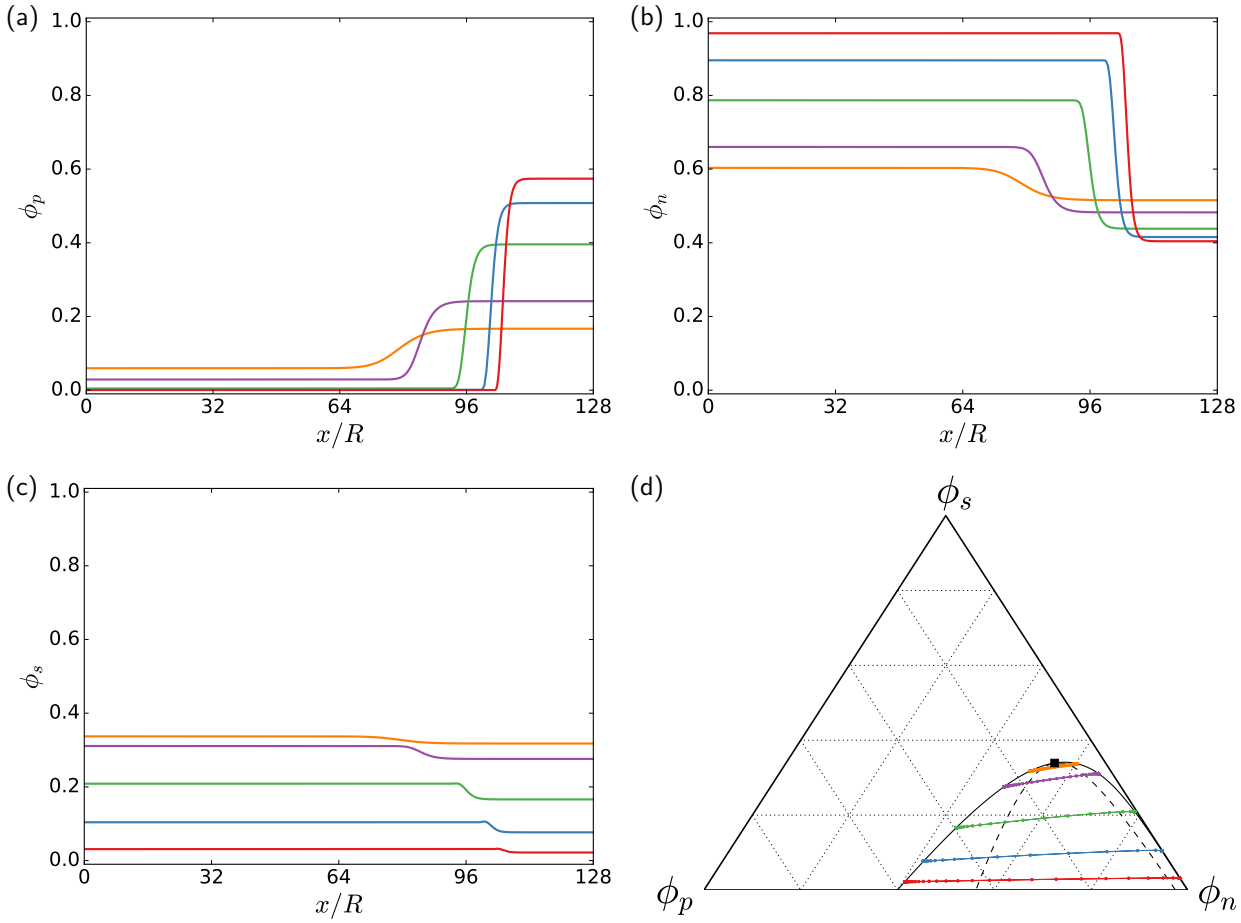

Figure 2: Plot of 1D volume-fraction profiles versus space of the (a) polymer, (b) non-solvent and (c) solvent. Each plot contains five different profiles whose average concentrations are: $\{\bar{\phi}_p, \bar{\phi}_n\} = \{0.1,\ 0.57\}$ (orange), $\{0.1,\ 0.6\}$ (purple), $\{0.1,\ 0.7\}$ (green), $\{0.1,\ 0.8\}$ (blue), $\{0.1,\ 0.87\}$ (red). Panel (d) gives a ternary phase diagram for $\chi = 0.912$ and $N = 50$. The solid line indicates the binodal, the dashed line indicates the spinodal and the filled square indicates the plait point.

binodal and a spinodal at $\chi = 0.912$ and $N = 50$, and is calculated numerically as outlined in the Supplemental Information. The multi-fluid model density profiles are obtained for the same χ and N, with $\kappa = 12$ and with average concentrations of $\{\bar{\phi}_p, \bar{\phi}_n\} = \{0.1,\ 0.57\}$, $\{0.1,\ 0.6\}$, $\{0.1,\ 0.7\}$, $\{0.1,\ 0.8\}$, $\{0.1,\ 0.87\}$. As is evident from Figure 2(d), the concentrations of ϕ_p and ϕ_n in the final domains are in excellent agreement with the phase diagram. This agreement holds across the range of concentrations in the figure for both weakly and strongly segregated domains.

In addition to the domain size and the equilibrium concentration, the width of the interfaces in the concentration profiles in Figure 2 are also variable. The interfacial width was calculated using the definition

$$l_i = \left| \frac{\phi_i^\beta - \phi_i^\alpha}{\partial\phi/\partial x} \right| \tag{51}$$

where ϕ_i^γ is the volume fraction of component i in the γ phase, and the spatial derivative $\partial\phi/\partial x$ is evaluated using a pseudo-spectral derivative at the midpoint of the interface. Qualitatively, we observe that the interfacial width is sharper as the distance from the plait point increases, and that the interface is asymmetric — being noticeably sharper near the polymer-lean phase than the polymer-rich phase. To gain insight into the behavior of the interfaces, we explore two possible theories.

The first is an adaptation of a strong-segregation theory by Broseta *et al.* for a binary polymer blend[63] to our model of a ternary polymer solution. Leaving the details of the derivation to the Supplemental Information, the theory predicts a characteristic width

$$l = l_\infty \left[1 - 2\ln 2 \left(\frac{1}{\chi N(1-\bar{\phi}_s)} + \frac{1}{\chi(1-\bar{\phi}_s)} \right) - \frac{2}{\chi(1-\bar{\phi}_s)} \left(\frac{1}{N} - 1 \right) + \ldots \right]^{-1/2} \tag{52}$$

where

$$l_\infty = \frac{1}{2} \left(\frac{\kappa}{\chi} \right)^{1/2} \tag{53}$$

is the leading-order width for asymptotic strong segregation and $\bar{\phi}_s$ is the average solvent concentration in the system.

Eq. 52 provides an intuitive and seemingly plausible explanation for interfaces. The width, l, depends mainly on two parameters: the gradient coefficient, κ, which widens interfaces at large values and the interaction strength, χ, which narrows them when it is large. Finite polymer lengths and the average polymer concentration, $\bar{\phi}_s$ introduce important corrections to l_∞, which converge relatively slowly.

The second theory is a weak-segregation theory that can be simply derived from scaling arguments from critical phenomena. Near the critical point, the interfacial width must scale as,

$$l \sim l_\infty \left(\chi^*\right)^{-\nu} \tag{54}$$

where

$$\chi^* = \frac{\chi - \chi_c}{\chi_c} \tag{55}$$

is a reduced Flory parameter, and $\nu = 1/2$ is the mean-field exponent.

To predict the interfacial width using Eq. 54, one needs to obtain a value for χ_c. For a given system with average concentrations $\{\bar{\phi}_p, \bar{\phi}_n\}$, χ_c corresponds to the value of the lowest χ where phase separation occurs at a *fixed solvent volume fraction*. Note that this does not correspond to the plait point on a fixed-χ ternary phase diagram.

To illustrate this distinction, Figure 3(a) shows the spinodal envelope for an example polymer ($N = 30$), the critical line that lies along the spinodal envelope and a plane that intersects both of these curves at $\chi = 1.4$. The plait point in a ternary diagram occurs where the critical line intersects with the plane of constant χ. The value of χ_c to be used in Eq. 55 is found by the intersection of a slice at constant ϕ_s that passes through $\{\phi_p, \phi_n\}$ and the critical line. We calculate χ_c numerically, using methods described in the Supplemental Information.

Table 2: Parameters used to obtain the data in Figure 3(b). $\chi_c^b = \frac{1}{2}\left(\frac{1}{\sqrt{N}} + 1\right)^2$, the critical point for a binary solution of polymer and non-solvent.

N	κ	χ/χ_c^b
1	1	{1.2, 1.4, 1.6}
2	2	1.4
5	{2, 4}	1.4
10	{1, 2, 4}	1.4
20	{1, 4, 8}	{1.2, 1.4, 1.6}
50	{10, 12, 15, 20, 30}	{1.4, 1.6}
80	{15, 20, 30, 40}	{1.2, 1.4, 1.6}
100	{20, 30, 40}	{1.2, 1.4, 1.6}

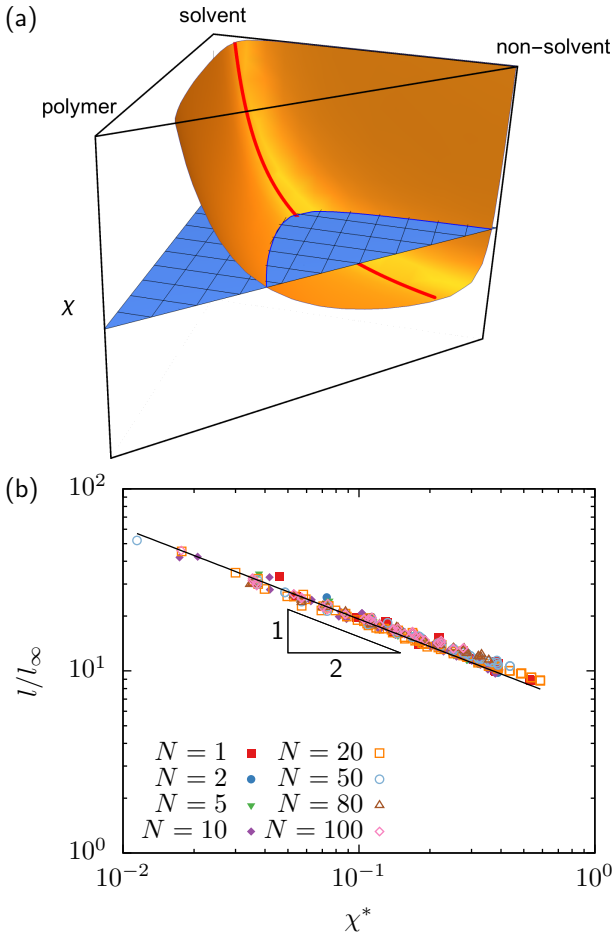

Figure 3: (a) Plot of the spinodal (orange), critical line (red) and a plane of $\chi = 1.4$ for a polymer with $N = 30$. (b) Plot of the scaled interfacial width (l/l_∞) versus reduced Flory parameter (χ^*) for variable N, κ and χ. The solid line is a fit to the data with slope 1/2.

Armed with both theories, Figure 3(b) shows the interfacial width obtained from simulating equilibrium configurations for a number of different N, κ and χ given in Table 2. The equilibrium configurations were obtained by the same process described above for Figure 2. The data in Figure 3(b) collapse completely to a universal (N-independent) power-law with exponent $-1/2$, clearly favoring the scaling theory. By contrast, the perturbation theory predicts that different values of N will not collapse, violating the observed behavior in Figure 3(b).

Upon inspection of the data it is likely that the disagreement with the perturbation theory is at least in part due to the low value of χ^* and the moderate values of N, which is far from the strong-segregation limit. (Note however that $\chi^* \ll 1$ does not necessarily imply that $\chi \ll 1$. Indeed this is not the case for many of the data points in the figure.) Further evidence that a small χ may explain the disagreement with the strong segregation theory comes from the observed deviation of the data from the $-1/2$ exponent at the largest values of χ^*. Unfortunately, we are unable to stabilize the calculation to high enough values of χ^* to test the possibility that the perturbation theory becomes valid in this range.

Also, unlike the scaling theory, the perturbation theory assumes that the solvent partitions equally between both phases. This assumption is clearly violated by the asymmetric system, as is evident in Figure 2.

There is one more intriguing possibility, suggested by the correspondence of the functional forms of Eq. 52 and Eq. 54. Expanding $(\chi - \chi_c)/\chi_c$ at high segregation-strength and substituting the resulting expression into Eq. 54 gives an equation very similar to Eq. 52, but with some missing terms. This suggests that it may be possible that both theories correspond in some region of the parameter space (e.g. when $\chi \sim \mathrm{O}(1)$ and $N \gg 1$).

Kinetics

The Doi-Onuki formalism predicts a mutual diffusion coefficient matrix from the friction coefficients and the free energy functional, and assures that our model obeys Onsager relations.

Note that the formalism is not limited to the simple friction coefficients that we employed in our derivation. However, when using a more complicated set of friction coefficients, one must be cognizant of the resulting stress division between the components. This issue is especially critical for two-fluid models with viscoelasticity.[52,64]

Many authors have worked on theories of mutual diffusion coefficients of polymer solutions[65] and blends[66] with the goal of obtaining quantitatively accurate predictions that match experimental data. As we discussed with the Flory–Huggins terms used in the free energy, we do not expect our model to quantitatively match experimental data without additional model complexity and careful parameter fitting. Furthermore, we caution that our model is very simple, and we are omitting physics that becomes important at large polymer concentration. However, we do expect our approach to yield qualitatively reasonable dynamics in the dilute polymer limit.

The Fickian diffusion matrix of the multi-fluid model is given by the product of the mobility and Hessian matrices,

$$D_{ik} = \sum_{j,k}^{p,n} M_{ij} H_{jk}. \tag{56}$$

Specifically, for the incompressible ternary system, the components of the mutual diffusion matrix are:

$$D_{pp} = \frac{k_B T}{\zeta_0}\left[\frac{1-\phi_p}{N_p} + \frac{\phi_p}{N_s} - 2\phi_p(1-\phi_p)\chi_{ps} - \phi_n\phi_p\chi_{pns}\right] \tag{57a}$$

$$D_{pn} = \frac{k_B T}{\zeta_0}\left[\frac{\phi_p}{N_s} - \frac{\phi_p}{N_n} + 2\phi_n\phi_p\chi_{ns} + \phi_p(1-\phi_p)\chi_{pns}\right] \tag{57b}$$

$$D_{np} = \frac{k_B T}{\zeta_0}\left[\frac{\phi_n}{N_s} - \frac{\phi_n}{N_p} + 2\phi_n\phi_p\chi_{ps} + \phi_n(1-\phi_n)\chi_{pns}\right] \tag{57c}$$

$$D_{nn} = \frac{k_B T}{\zeta_0}\left[\frac{1-\phi_n}{N_n} + \frac{\phi_n}{N_s} - 2\phi_n(1-\phi_n)\chi_{ns} - \phi_n\phi_p\chi_{pns}\right]. \tag{57d}$$

From Equation 57 we recover Rouse diffusion in the dilute polymer limit,

$$\lim_{\phi_p \to 0} D_{pp} = \frac{k_B T}{\zeta_0 N_p} \tag{58}$$

$$\lim_{\phi_p \to 0} D_{pn} = 0 \tag{59}$$

and simple monomer diffusion in the dilute non-solvent limit,

$$\lim_{\phi_n \to 0} D_{nn} = \frac{k_B T}{\zeta_0 N_n} \tag{60}$$

$$\lim_{\phi_n \to 0} D_{np} = 0 \tag{61}$$

Figure 4 shows the four components of the mutual diffusion coefficient for pseudo-binary parameters $N = 50$ and variable χ at a constant solvent concentration. (Recall $\chi = \chi_{pn}$, $\chi_{ps} = \chi_{ns} = 0$). In Figure 4, we set $\phi_s = 0.1$, but the qualitative behavior is similar for any value of ϕ_s.

When $\chi = 0$, terms that precede polymer concentration gradients (D_{pp} and D_{np}) depend linearly on concentration. Diffusion coefficients that precede non-solvent gradients (D_{pn} and D_{nn}) are constants.

At finite χ the quadratic terms in Equations 57a–57d are negative for the diagonal components (D_{pp} and D_{nn}), decreasing the diffusivity at intermediate concentrations. By contrast, the quadratic terms in the off-diagonal components (D_{pn} and D_{np}) are positive. This difference has important implications for the behavior of the model, since — at a large enough χ — the off-diagonal terms can dominate diffusion at intermediate concentrations. This could play an important role in the dynamics of phase-separated systems (e.g. late-stage coarsening), where the bulk diffusion of polymer-rich and non-solvent-rich phases is slow, but the diffusion at interfaces is not.

When χ is sufficiently large, the diagonal components become negative. Negative diffusion coefficients are of course possible because the system undergoes phase separation under such conditions. One should note that because there is no stochastic element to our equations of motion, the system is unable to overcome nucleation barriers by thermal fluctuation. Therefore spinodal decomposition is the only spontaneous phase separation mechanism pos-

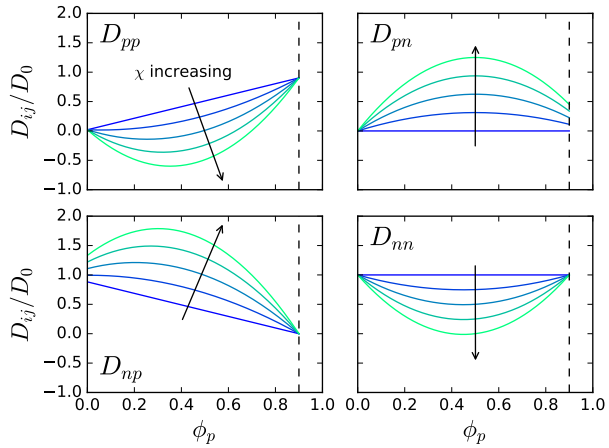

Figure 4: The components of the mutual diffusion coefficient versus ϕ_p for $N = 50$ at constant $\phi_s = 0.1$ and $\chi = \{0, 1.25, 2.5, 3.75, 5\}$ (blue to green). Diffusion coefficients are scaled by the monomer diffusion, $D_0 = k_B T/\zeta_0$.

sible when quenching a nearly homogeneous state (i.e., when the initial state contains no inhomogeneities larger than the critical nucleus size).[67]

Spinodal decomposition kinetics are vitally important to membrane structure, and studying them provides one of our primary motivations for the development of our model. For example, the key assumption behind several important mass-transfer models of membrane formation is that the phase separation process in a film with an inhomogeneous polymer distribution is responsible for the asymmetric pore structure of many membranes.[9,10] While this mechanism is popular and intuitive, it has not been rigorously tested. Analyzing the phase separation kinetics as a function of homogeneous polymer and non-solvent concentration is a first step towards a quantitative evaluation of this assumption.

For the moment, we focus our attention on the spinodal decomposition kinetics of a bulk ternary polymer solution. A great deal is already known about the kinetics of bulk spinodal decomposition. Binary systems have been widely studied (e.g.[68]), and there are already several computational studies of ternary systems, including ternary polymer solutions.[12,69,70]

We begin our study of the spinodal decomposition kinetics with a linear stability analysis (LSA) of the diffusion equation in Eq. 18. Leaving the details of the derivation to the Supplemental Information, the LSA reveals that at short times, the thermodynamic instability

is characterized by exponential growth of an eigenmode ψ,

$$\delta\psi(\boldsymbol{q},t) = \exp[\lambda_+(\boldsymbol{q})t] \tag{62}$$

where λ_+ is a wave-vector dependent eigenvalue of the diffusion equation. The exponential growth is dominated by the largest, fastest-growing mode, q_m, which proceeds at a rate $\lambda_m = \lambda_+(q_m)$.

For the general set of model parameters described above, both q_m and λ_m must be calculated numerically. However, the pertinent trends can be captured if one assumes a scalar mobility, $M_{ij} = M\delta_{ij}$, and square-gradient coefficient, $K_{ij} = \kappa\delta_{ij}$. In this case, the fastest growing mode reduces to a function of the thermodynamic parameters alone,

$$q_m^2 = \frac{1}{4\kappa}\Bigg[-\left(\bar{H}_{pp} + \bar{H}_{nn}\right) + \sqrt{\left(\bar{H}_{pp} - \bar{H}_{nn}\right)^2 + 4\bar{H}_{pn}\bar{H}_{np}}\Bigg] \tag{63}$$

where $\bar{H}_{ij}$ are the components of the Hessian matrix in Eq. 23 evaluated at the average concentration. The spinodal decomposition rate is given by,

$$\lambda_m = M\kappa q_m^4. \tag{64}$$

Figure 5 shows the magnitude of q_m as a density plot on a ternary phase diagram using the pseudo-binary parameters introduced previously. Figure 5 shows that near the boundaries of the spinodal, q_m goes to zero, meaning the early-time demixing characteristic domain size, $2\pi/q_m$, diverges. Conversely, for quenches deep into the spinodal, q_m is large, resulting in small early-time domains.

These results have important ramifications for membrane formation, giving support to the hypothesis that an inhomogeneous polymer film can lead to asymmetric membranes. Indeed,

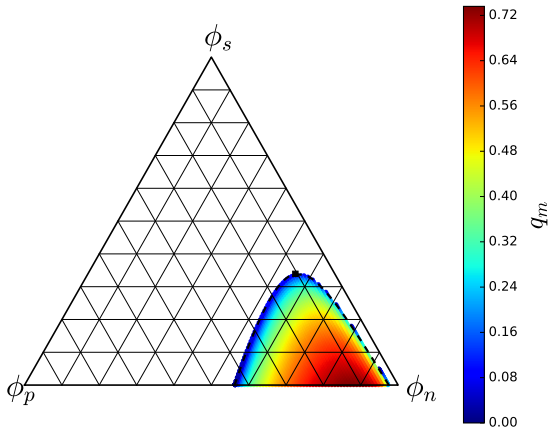

Figure 5: Magnitude of the fastest growing mode (in units of R^{-1}) overlaid on the ternary phase diagram using pseudo-binary model parameters ($N = 50$, $\chi = 0.912$, $\kappa = 12$). For clarity, the binodal curve is omitted from the phase diagram.

according to Figure 5, if the polymer layer develops inhomogeneities before demixing, then regions of the film with concentrations near the edge of the spinodal should decompose into large domains, and regions that are deeply quenched should give rise to small domains. This intuition agrees with the asymmetry observed in membranes; smaller pores are formed near the non-solvent/polymer interface, where the quench is presumed to be deeper.

The story gets more complicated however when we consider the rate of decomposition. The rate, λ_m, is proportional to q_m^4, and therefore deeper quenches demix much faster than shallow ones. As a consequence, smaller domains may de-mix and coarsen before large domains can de-mix, promoting more symmetric systems. Because both effects are counter-posed, it is not obvious from the LSA whether symmetry or asymmetry will prevail.

While the linear analysis cannot capture the effects of coarsening, our numerical methods can. Therefore, we performed simulations of 2D systems at various uniform average initial concentrations undergoing spinodal demixing and coarsening both with and without hydro-dynamics. (The initial conditions were purturbed by a small amount of uniformly distributed random noise with amplitude $\epsilon = 10^{-2}$ to initiate the decomposition.) While it is trivially possible with our methods to do 3D calculations, we chose to work in 2D because we have access to larger simulation cells due to memory constraints. Admittedly, some of the details

of the dynamics will differ because of the dimensionality, but two dimensions are adequate for a first characterization of the model and numerical methods.

For the calculations that follow, we use the pseudo-binary model parameters described previously and calculate a characteristic domain size by examining the first moment of the normalized polymer structure factor,[24,71]

$$\langle q \rangle = \frac{\sum_q q\, s_p(q,t)}{\sum_q s_p(q,t)} \tag{65}$$

where the structure factor

$$s_p(q,t) = \frac{1}{\int d\Omega} \int d\Omega\, \mathcal{F}\left[\frac{g_p(\boldsymbol{r},t)}{g_p(0,t)}\right] \tag{66}$$

is given by the Fourier transform of the polymer density correlation function,

$$g_p(\boldsymbol{r},t) = \left\langle \int d\boldsymbol{r}' \left[\phi_p(\boldsymbol{r}+\boldsymbol{r}',t)\phi_p(\boldsymbol{r}',t) - \langle\phi_p\rangle^2\right] \right\rangle \tag{67}$$

averaged over the solid angles $d\Omega$ of $\boldsymbol{q}$ with $q \equiv |\boldsymbol{q}|$.

Figure 6 shows the characteristic polymer domain size versus time for three systems with different average concentrations inside the spinodal, where hydrodynamic effects are omitted from the simulation. Figure 6(a) shows the raw domain size versus time, whereas Figure 6(b) shows the same data, with the ordinate normalized by q_m and the abscissa normalized by λ_m. There are two distinct regimes. At early times, the domain size grows and approaches a steady value. This early-time regime is the linear regime, and quantitatively matches the prediction of the LSA. The quantitative agreement can be seen by observing that the different early-time domain sizes that are apparent in Figure 6(a), collapse to a single curve in Figure 6(b) when q and t are normalized by the values predicted by the LSA. Indeed, the scaled domain size at early times collapses to $q_m/\langle q\rangle \approx 1$, and the inflection point marking the regime change occurs at $\lambda_m t \approx 1$ when we use a value of $M = 1$ for the scalar mobility.

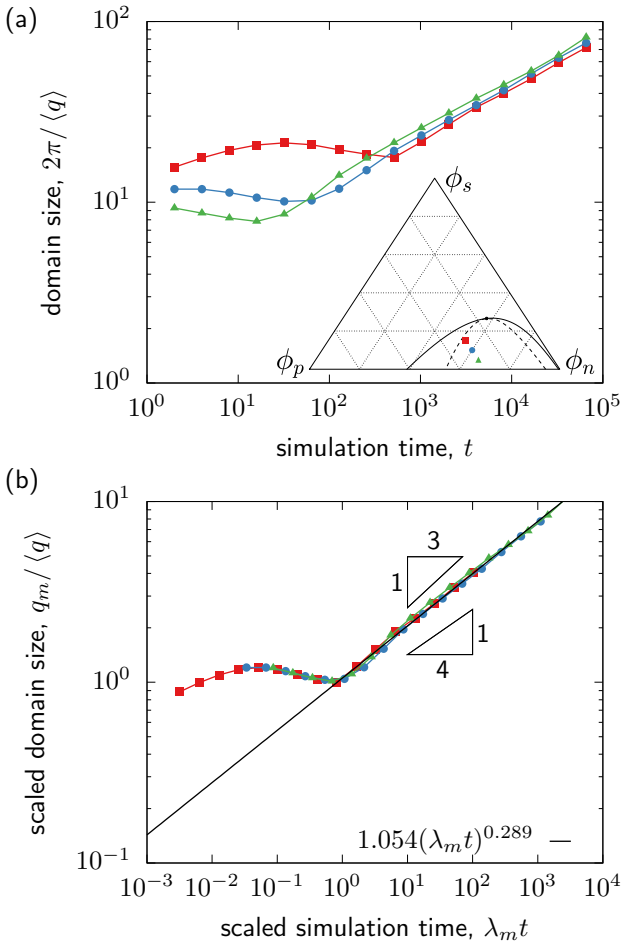

Figure 6: (a) The characteristic domain size, $2\pi/\langle q \rangle$, obtained from the first moment of the polymer structure factor for an isotropic ternary mixture undergoing spinodal decomposition for $N = 20$, $\kappa = 2$ and $\chi = 0.973$. The inset shows the average concentrations of each of the three curves overlaid on the ternary phase diagram: $\{\phi_p, \phi_n\} = \{0.3,\ 0.55\}$ (red squares), $\{0.3,\ 0.60\}$ (blue circles), $\{0.3,\ 0.65\}$ (green triangles). (b) Same data as panel above, normalized by q_m from Eq. 63 and λ_m from Eq. 64 (with $M = 1$).

(This choice of the mobility reflects the fact that we have non-solvent droplets in majority polymer domains, and the dilute solution diffusivity is equal to the monomer diffusivity.)

At late times, we cross over to a coarsening regime with domains that grow according to a power law $\langle q \rangle^{-1} \sim t^n$. A fit to the data yields an effective coarsening exponent of $n = 0.289$. Coarsening behavior (i.e. Ostwald ripening) is of course not described by the LSA, but by the theory of Lifshitz, Slyozov and Wagner (LSW).[72,73] Our observation of a power-law is consistent with the theory, but our observed exponent is clearly less than the 1/3 predicted by LSW.

The minor apparent disagreement with the LSW theory is not surprising, and can be readily explained. The theory is strictly valid only at long times and in the limit of a dilute minority species with spherical droplets.[72–74] The data in Figure 6 do not satisfy these conditions, which in fact can be difficult to reach computationally. Accordingly, many other computational studies of purely diffusive coarsening have observed an effective scaling exponent less than 1/3. For instance, simulations of symmetric systems at the critical composition with a concentration-dependent mobility are observed to give an exponent equal to 1/4,[24,75] demonstrating the dominance of surface diffusion over bulk diffusion.[76,77] Additionally, coarsening rates for systems with a concentration-dependent mobility away from the critical composition, are consistently reported with exponents less than 1/3.[71,78–83] Since surface diffusion cannot be invoked as a mechanism in the latter case, it is widely believed that slow bulk diffusion is responsible for a protracted transition to the long-time behavior.

Our data, which comes from an asymmetric system and consists of non-solvent droplets in a polymer matrix, has a coarsening exponent ($n = 0.289$) which is consistent with literature values for off-critical mixtures. Visual inspection of the volume fraction profiles provides qualitative evidence that bulk diffusion is indeed slow, supporting the prevailing view. Plots of the scaled structure factor are provided in Figure S1 of the Supplemental Information showing that dynamic scaling is obeyed at long times, giving further evidence that the results contained in Figure 6 are not simulation artifacts.

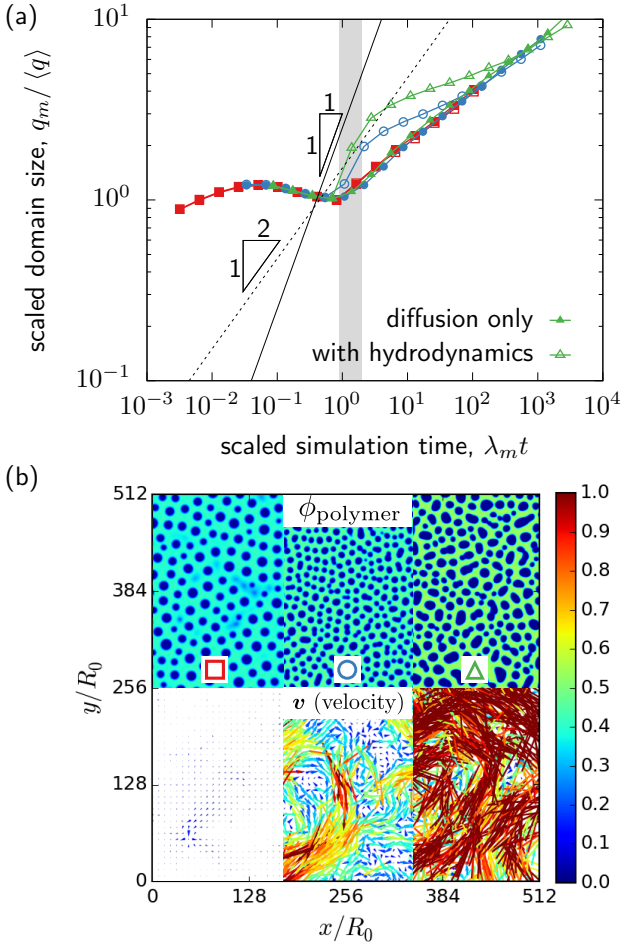

Figure 7: (a) The scaled domain size versus scaled time for an isotropic ternary mixture undergoing spinodal decomposition with hydrodynamics (open symbols) and without hydrodynamics (closed symbols) for the same parameters and compositions as Figure 6. Scaling laws of t^1 and $t^{1/2}$ are given for comparison. (b) Real space plots of the polymer volume fraction (upper half) and velocity fields (lower half) for a section of each of the three compositions at the time indicated by the gray bar in panel (a). The color bar scale is the same for both the density and velocity plots.

The inclusion of hydrodynamic effects adds additional complexity to the bulk spinodal demixing kinetics, as shown in Figure 7. For simplicity, the mixture viscosity is fixed to a constant value equal to the reference viscosity, which is chosen to be the viscosity of the solvent. Figure 7(a) gives the scaled domain size versus the scaled simulation time for the same compositions shown in Figure 6. Again, the early-time linear demixing regime agrees between all cases when appropriately scaled.

The late-stage coarsening behavior is more interesting. For the system with the smallest volume fraction of the non-solvent minority phase, the domain size in the calculation with hydrodynamics closely mirrors the domain sizes obtained without hydrodynamics. However, with an increasing volume fraction of the minority phase, the domain size at intermediate times begins to diverge from the data describing diffusive coarsening. Finally, at late times, there is no effect due to hydrodynamics, and the data again fall onto a universal curve with the same exponent seen in Figure 6.

The cause of this deviation can be seen by looking at Figure 7(b), which shows a portion of the morphology and velocity field for each composition at the first time-point immediately following the transition to coarsening. For the system with the smallest non-solvent volume fraction, the non-solvent droplets are almost perfectly circular, and there is very little flow. By contrast, the system with the largest non-solvent volume fraction has more elongated domains and a significant flow field.

These observations are consistent with Siggia's hydrodynamic coarsening mechanism, where interfacial tension in non-spherical domains drives flow to give a coarsening rate of $\langle q \rangle^{-1} \sim t$.[52,84–86] Indeed, while the regime in these examples is quite short in duration, the initial coarsening exponent for the simulation with the largest non-solvent volume fraction is consistent with a scaling exponent of 1. Additionally, the surface tension-driven flows that cause coarsening in Siggia's mechanism are only possible for non-spherical domains,[52] which matches our observation of the morphology and velocity fields in Figure 7(b). Because Siggia's mechanism only applies to non-spherical geometries, one typically associates it with

a bi-continuous system, which can maintain non-spherical domains indefinitely. Interestingly, our simulations show that the mechanism still applies to a droplet morphology, but the effect is transient.

San Miguel has argued that Siggia's mechanism is not valid in two dimensions, and that there should be instead a coarsening rate proportional to $t^{1/2}$ associated with either interfacial diffusion or droplet coarsening.[87] We see no evidence of a 1/2 scaling exponent, but in defense of San Miguel's arguments we have neither a bi-continuous morphology to enable interfacial diffusion nor thermal noise to permit coalescence of the droplets by the Brownian diffusion. In a simulation of a symmetric, binary system with an FHG functional and hydrodynamics, Chen and Chakrabarti report coarsening rates consistent with the 1/2 scaling exponent at the critical composition, but report greater than 1/2 scaling at intermediate times off the critical axis.[88] These latter results off the critical composition are qualitatively similar to ours, with domains sizes that approach the LS scaling at long times.

The convergence of bulk coarsening rates at late times in Figures 6 and 7 suggests that coarsening will counteract concentration gradients and promote symmetric domain sizes in a NIPS process. This is a consequence of the fact that there is only a single length scale (the domain size) and that diffusion dominates at long times. Thus, a deeply-quenched system that initially forms small domains quickly coarsens by the same diffusive mechanisms that cause a system at a shallow quench to form large domains. This does not, of course, prove that an initially inhomogeneous film is unimportant in the generation of asymmetric membranes. Rather, it shows that the formation mechanism of an asymmetric membrane must depend on more phenomena than diffusion and constant viscosity hydrodynamics.

The phase-field model we have defined in this manuscript is sufficiently general that we may yet gain more insight from bulk coarsening behavior into this formation mechanism. We anticipate that morphologies spanning from majority non-solvent to majority polymer will coarsen at different rates due to the contrast in mobilities and viscosities, which may have important consequences for the formation mechanism of asymmetric membranes. However,

the bulk coarsening phenomena defined by our ternary model is significantly more complex than we have space to explore here and warrants a separate study.

To conclude our preliminary investigation of the kinetics of the multi-fluid model, we examine a quench into the spinodal near a polymer solution/non-solvent interface. To simulate an interface between the non-solvent bath and polymer solution with periodic boundary conditions we use an initial condition that (i) is symmetric across the midpoint in the y-direction to give a no-flux boundary condition from symmetry and (ii) has a (rounded-off) step in concentration creating an interface between a polymer solution in the inner region and a non-solvent bath in the outer region.

For this example, the polymer solution is initialized with a volume fraction already inside the spinodal region (again with a small amount of noise). For comparison purposes, the model parameters and initial condition of the polymer solution are the same as those in the bulk study. However, unlike the bulk study, mass transfer immediately begins exchanging solvent in the film with non-solvent in the bath. Clearly in a true NIPS process, the polymer solution does not begin in the spinodal, but is instead driven there inhomogeneously by mass transfer.[10] However, this process is non-trivial, and we set it aside as future work.

Figure 8 shows the evolution of the non-solvent volume fraction where the lower (symmetric) half of the plot and a portion of the non-solvent bath has been omitted. Figure 8 also shows the velocity vector field at $t = 50$.

The introduction of an interface breaks the symmetry of the system, leading to a surface-directed spinodal decomposition (SDSD) process.[89,90] The signature spinodal wave of SDSD can be clearly seen in Figure 8(a)-(c) propagating from the interface into the bulk of the film. As predicted by Ball and Essery, and in harmony with our LSA for the bulk system, both the speed of the wave front and the domain size depend on the quench depth. This can be qualitatively confirmed by inspection of Figure 8, where the quench depth of c > b > a. Thus the wave front velocity of c > b > a as shown for all compositions at $t = 25$ and the initial domain size of a > b > c as seen by comparing composition (b) at $t = 75$ and

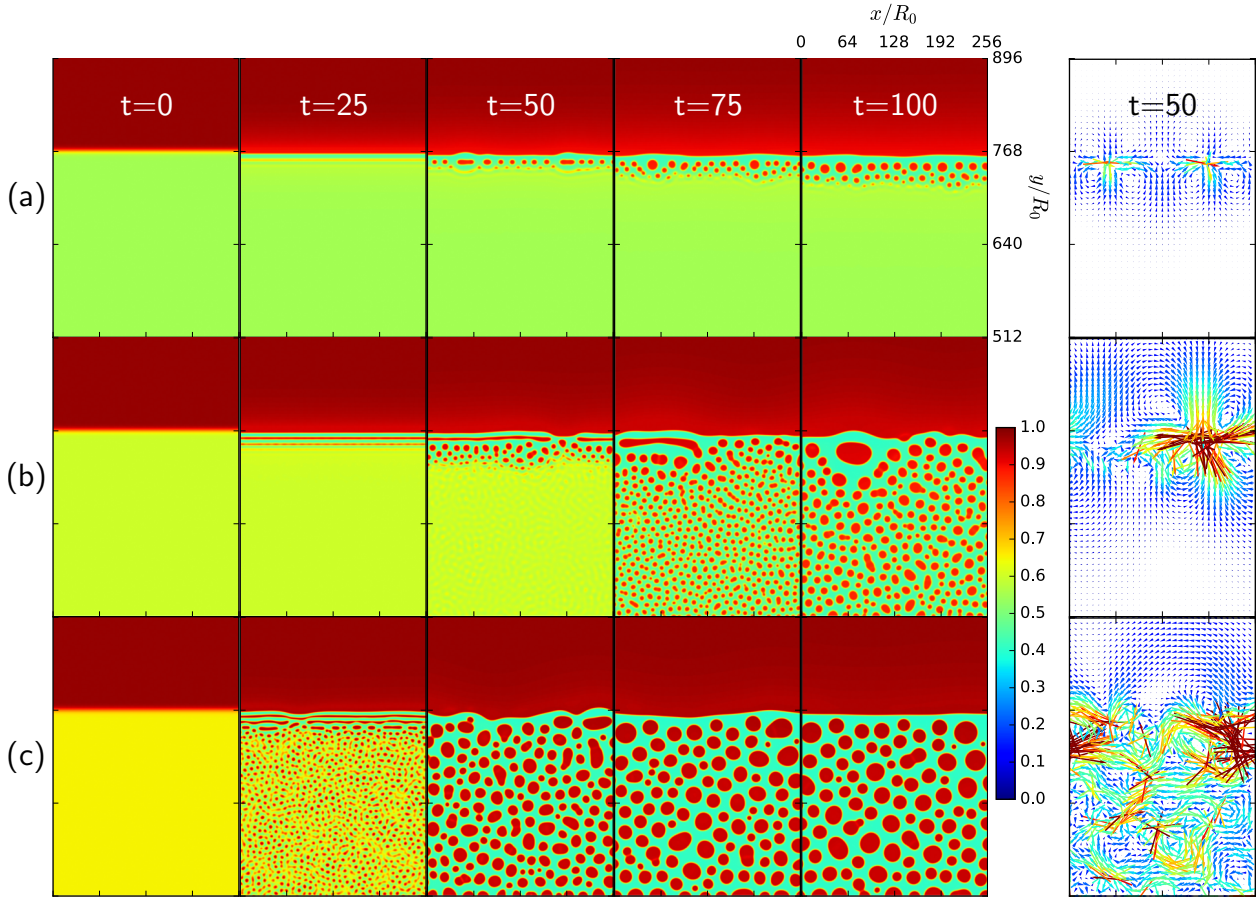

Figure 8: Spinodal decomposition near a polymer solution/non-solvent bath interface for $N = 20$, $\kappa = 2$ and $\chi = 0.973$. The density plots on the left show the non-solvent volume fraction for $t = \{0, 25, 50, 75, 100\}$. The velocity field for $t = 50$ is shown on the right. The outer concentration is essentially pure non-solvent: $\phi_p = 0.01, \phi_n = 0.98$. The inner concentration is: $\{\phi_p, \phi_n\} = \{0.3, 0.55\}$ (a), $\{0.3, 0.60\}$ (b), $\{0.3, 0.65\}$ (c). The symmetric bottom half and a portion of the non-solvent bath has been cut from the figure for clarity. (The simulation box contains 256×1024 collocation points).

composition (c) at $t = 25$. Interestingly, the influence of the surface only propagates a finite distance into the film, and bulk spinodal decomposition is observed away from the interface at a time slightly delayed relative to the SDSD wave propagation. The finite propagation distance of this wave is certainly a consequence of the competition between the demixing rate of the bulk of the film (which is initialized in the unstable region) and the demixing due to the spinodal wave induced by the presence of the interface.

One of our primary interests is the generation of asymmetric structures. At early times, the structure is clearly non-uniform due to the SDSD process. In fact, an early-time morphology similar to Figure 8(c) at $t = 25$ has been observed in a phase-field model by Zhou and Powell, who claim that such structures compare favorably to experimental micrographs of asymmetric membranes.[12] There are several criticisms one can make of this claim, namely that the apparent agreement between simulation and micrograph is actually rather poor, the length scales of the simulation and experimental features are very different and that the morphology was obtained by an unphysical quench into the spinodal.

Furthermore, from the longer time morphologies in Figure 8, it appears that simply the presence of an interface with a non-solvent bath does not create any lasting asymmetric domain sizes. As was the case in the bulk, the key principle to returning to uniform domain sizes is again the rapidity of coarsening. For instance, in Figure 8(b) we observe at $t = 75$ that the initial SDSD wave has already begun to coarsen, and that the domains near the film/bath interface are larger than those deeper in the bulk-like region. This is actually an inverted domain size gradient to what is observed in asymmetric membrane formation — large domains near the interface and small domains in the bulk. However, by $t = 100$ the entire film has had sufficient time to coarsen, and the domains are practically uniform (except for one large domain that remains). The more deeply quenched and rapidly developing case in Figure 8(c) confirms that the domains are indeed uniform at long times. Thus to truly understand the origin of pore gradients, it seems that we will likely need to understand the coarsening process and how it can be arrested either by viscosity and mobility contrast

among phases or possibly viscoelasticity.

Finally, we note an interesting phenomenon that can be seen in the non-solvent density plot and velocity vector plot in Figure 8 at $t = 50$. Once spinodal decomposition is underway, hydrodynamic flows perturb the film/bath interface, causing it to transiently roughen before settling to a new smooth profile at long times. The origin of this roughening appears to be surface-tension induced flow, similar to Siggia's hydrodynamic coarsening mechanism. Experiments on the spinodal decomposition of thin-films of isotopic polymer blends have shown a similar transient roughening that is attributed to hydrodynamic flow,[91] and Zhou and Powell also noted the impact of hydrodynamic flows on the near-surface morphology in their phase-field simulations.[12] A full exploration of this effect and its relation to membrane morphologies is deferred to later work.

Summary and Conclusion

We have presented a multi-fluid model of a ternary polymer solution with the goal of better understanding the formation of microstructure in polymer membranes. Using a formalism introduced by Doi and Onuki,[1] we developed a model rigorously founded on fundamental polymer thermodynamics with mobility coefficients that obey Onsager relations. We presented an efficient pseudo-spectral method for both the diffusion and momentum equations. The diffusion equation is solved using a semi-implicit scheme to overcome the numerical stiffness associated with higher-order derivatives in the diffusion equation. The inertia-less momentum equation is solved by a method that we developed with the capability of treating variable-viscosity fluids. Applying these methods on modern compute hardware, we are able to access systems with micron length scales and millisecond time scales with relative ease.

Following the model and method development, we characterized the thermodynamic and kinetic properties of the model. The equilibrium concentrations give excellent agreement with the related ternary phase diagram, and the interfaces show behavior consistent with mean-

field behavior in the vicinity of the critical point. The Fickian mutual diffusion coefficients are consistent with the self-diffusion coefficients in the requisite limits, and — as one would expect — are sensitive to the thermodynamic parameters.

We also examined the kinetics of spinodal decomposition by performing both a linear stability analysis and full two-dimensional numerical simulations. Using the linear stability analysis, we show that there is a single length scale ($2\pi/q_m$) and a single time scale ($1/\lambda_m$) that characterize bulk demixing kinetics, which are in quantitative agreement with short-time results from our numerical calculations. Long-time coarsening kinetics for a purely diffusive model give an effective scaling exponent of $n = 0.289$, lower than the 1/3 predicted by Lifshitz, Slyozov and Wagner, but consistent with scaling exponents reported in the literature for off-critical mixtures with slow bulk diffusion. When hydrodynamics are included, a scaling exponent of 1 is observed, which is consistent with the mechanism proposed by Siggia.[84] Regardless of whether or not hydrodynamics are included, long-time domain sizes converge to a universal curve, indicating the tendency of the system to approach uniform domain sizes.

In addition to bulk spinodal demixing kinetics, we briefly examined the spinodal decomposition of a film in the presence of an interface with a non-solvent bath. We observe behavior characteristic of surface-directed spinodal decomposition, and again confirm the importance of coarsening on the morphology.

We look forward in future work to a more detailed study of late-stage coarsening kinetics when there is a large contrast between the mobility and viscosity of polymer and non-solvent phases, in an effort to understand how the pore structure of membranes "freeze." Additionally, we are interested in an investigation of the role that mass transfer plays in the phase separation process, and we would also like to investigate the hydrodynamic mechanisms that lead to an apparent surface roughness at the film/bath interface.

Acknowledgement

We would like to acknowledge financial support from Asahi Kasei Co. and Dow Chemical. Additionally, we acknowledge computational resources from the Center for Scientific Computing from the CNSI, MRL: an NSF MRSEC (DMR-1121053) and NSF CNS-0960316. HDC would like to acknowledge partial support from the National Science Foundation under grant DMS-1317684.

References

(1) M. Doi and A. Onuki, *J. Phys. II France*, 1992, **2**, 1631–1656.

(2) A. J. McHugh and L. Yilmaz, *J. Polym. Sci. Pol. Phys.*, 1985, **23**, 1271–1274.

(3) *Membrane Separation Technologies to 2018*, The Freedonia Group technical report, 2015.

(4) P. van de Witte, P. Dijkstra, J. van den Berg and J. Feijen, *J. Membr. Sci.*, 1996, **117**, 1–31.

(5) H. Strathmann, K. Kock, P. Amar and R. Baker, *Desalination*, 1975, **16**, 179–203.

(6) I. Wienk, R. Boom, M. Beerlage, A. Bulte, C. Smolders and H. Strathmann, *J. Membr. Sci.*, 1996, **113**, 361–371.

(7) C. Smolders, A. Reuvers, R. Boom and I. Wienk, *J. Membr. Sci.*, 1992, **73**, 259–275.

(8) L. Yilmaz and A. J. McHugh, *J. Appl. Polym. Sci.*, 1986, **31**, 997–1018.

(9) A. Reuvers and C. Smolders, *J. Membr. Sci.*, 1987, **34**, 67–86.

(10) C. S. Tsay and A. J. Mchugh, *J. Polym. Sci. Pol. Phys.*, 1990, **28**, 1327–1365.

(11) B. F. Barton and A. J. McHugh, *J. Polym. Sci. B Polym. Phys.*, 1999, **37**, 1449–1460.

(12) B. Zhou and A. C. Powell, *J. Membr. Sci.*, 2006, **268**, 150–164.

(13) A. Akthakul, C. E. Scott, A. M. Mayes and A. J. Wagner, *J. Membr. Sci.*, 2005, **249**, 213–226.

(14) X.-L. Wang, H.-J. Qian, L.-J. Chen, Z.-Y. Lu and Z.-S. Li, *J. Membr. Sci.*, 2008, **311**, 251–258.

(15) X. He, C. Chen, Z. Jiang and Y. Su, *J. Membr. Sci.*, 2011, **371**, 108–116.

(16) B. F. Barton, P. D. Graham and A. J. McHugh, *Macromolecules*, 1998, **31**, 1672–1679.

(17) Y. Mino, T. Ishigami, Y. Kagawa and H. Matsuyama, *J. Membr. Sci.*, 2015, **483**, 104–111.

(18) P. G. de Gennes, *Macromolecules*, 1976, **9**, 587–593.

(19) J. G. E. M. Fraaije, *J. Chem. Phys.*, 1993, **99**, 9202–9212.

(20) G. H. Fredrickson, *J. Chem. Phys.*, 2002, **117**, 6810.

(21) D. M. Hall, T. Lookman, G. H. Fredrickson and S. Banerjee, *Phys. Rev. Lett.*, 2006, **97**, 114501.

(22) D. M. Hall, T. Lookman, G. H. Fredrickson and S. Banerjee, *J. Comput. Phys.*, 2007, **224**, 681–698.

(23) M. Müller and J. J. de Pablo, *Annu. Rev. Mater. Res.*, 2013, **43**, 1–34.

(24) V. E. Badalassi, H. D. Ceniceros and S. Banerjee, *J. Comput. Phys.*, 2003, **190**, 371–397.

(25) H. Ceniceros and G. H. Fredrickson, *Multiscale Model. Sim.*, 2004, **2**, 452–474.

(26) J. W. Cahn and J. E. Hilliard, *J. Chem. Phys.*, 1958, **28**, 258–267.

(27) P. C. Hohenberg and B. I. Halperin, *Rev. Mod. Phys.*, 1977, **49**, 435–479.

(28) G. H. Fredrickson, *The Equilibrium Theory of Inhomogeneous Polymers*, Oxford University Press, 2006.

(29) P. G. de Gennes, *The Journal of Chemical Physics*, 1980, **72**, 4756.

(30) M. Doi and S. F. Edwards, *The Theory of Polymer Dynamics*, Oxford University Press, 1986.

(31) R. G. Larson and H. Brenner, *Constitutive Equations for Polymer Melts and Solutions*, Butterworths, 1988.

(32) E. Helfand and G. H. Fredrickson, *Phys. Rev. Lett.*, 1989, **62**, 2468–2471.

(33) S. T. Milner, *Phys. Rev. E*, 1993, **48**, 3674–3691.

(34) M. Cromer, M. C. Villet, G. H. Fredrickson and L. G. Leal, *Phys. Fluids*, 2013, **25**, 051703.

(35) P. A. Vasquez, G. H. McKinley and L. Pamela Cook, *J. Non-Newton. Fluid*, 2007, **144**, 122–139.

(36) N. Germann, L. P. Cook and A. N. Beris, *J. Non-Newton. Fluid*, 2013, **196**, 51–57.

(37) N. Germann, A. Kate Gurnon, L. Zhou, L. Pamela Cook, A. N. Beris and N. J. Wagner, *J. Rheol.*, 2016, **60**, 983–999.

(38) M. Doi, *J Phys.-Condens. Mat.*, 2011, **23**, 284118.

(39) A. N. Beris and B. J. Edwards, *Thermodynamics of Flowing Systems with internal microstructure*, Oxford University Press, 1994.

(40) H. C. Öttinger, *Beyond Equilibrium Thermodynamics*, John Wiley and Sons, Inc., 2005.

(41) V. G. Mavrantzas and A. N. Beris, *J. Chem. Phys.*, 1999, **110**, 616–627.

(42) N. Germann, L. Cook and A. Beris, *J. Non-Newton. Fluid*, 2016, **232**, 43–54.

(43) L. D. Landau and E. M. Lifshitz, *Statistical Physics, Part 1*, Pergamon Press, 3rd edn., 1980, vol. 5.

(44) H. Tang and K. F. Freed, *J. Chem. Phys.*, 1991, **94**, 1572.

(45) P.-G. de Gennes, *Scaling concepts in polymer physics*, Cornell university press, 1979.

(46) U. M. Ascher, S. J. Ruuth and B. T. R. Wetton, *SIAM Journal on Numerical Analysis*, 1995, **32**, 797–823.

(47) M. Cromer, M. C. Villet, G. H. Fredrickson, L. Gary Leal, R. Stepanyan and M. J. H. Bulters, *J. Rheol.*, 2013, **57**, 1211–1235.

(48) D. Gottlieb and S. A. Orszag, *Numerical Analysis of Spectral Methods*, Society for Industrial and Applied Mathematics, 1977.

(49) J. H. Ferziger and M. Perić, *Computational Methods for Fluid Dynamics*, Springer, 2002.

(50) C. Canuto, M. Y. Hussaini, A. Quarteroni and T. A. Zang, *Spectral Methods in Fluid Dynamics*, Springer, 1988.

(51) S.-M. Hur, C. J. García-Cervera and G. H. Fredrickson, *Macromolecules*, 2012, **45**, 2905–2919.

(52) H. Tanaka, *J. Phys.-Condens. Mat.*, 2000, **12**, R207.

(53) R. B. Thompson, K. O. Rasmussen and T. Lookman, *J. Chem. Phys.*, 2004, **120**, 31.

(54) K.-C. Ng, *J. Chem. Phys.*, 1974, **61**, 2680.

(55) K. T. Delaney and G. H. Fredrickson, *Computer Physics Communications*, 2013, **184**, 2102–2110.

(56) W. H. Press, S. A. Teukolsky, W. T. Vetterling and B. P. Flannery, *Numerical Recipes in C*, Cambridge University Press, 1992.

(57) P. Grzywacz, J. Qin and D. Morse, *Phys. Rev. E*, 2007, **76**, 061802.

(58) C. C. Han, B. J. Bauer, J. C. Clark, Y. Muroga, Y. Matsushita, M. Okada, Q. Tran-cong, T. Chang and I. C. Sanchez, *Polymer*, 1988, **29**, 2002–2014.

(59) D. C. Morse and J. K. Chung, *J. Chem. Phys.*, 2009, **130**, 224901.

(60) F. W. Altena and C. A. Smolders, *Macromolecules*, 1982, **15**, 1491–1497.

(61) C. Cohen, G. B. Tanny and S. Prager, *J. Polym. Sci. Polym. Phys. Ed.*, 1979, **17**, 477–489.

(62) L. Bronsard and R. V. Kohn, *Communications on Pure and Applied Mathematics*, 1990, **43**, 983–997.

(63) D. Broseta, G. H. Fredrickson, E. Helfand and L. Leibler, *Macromolecules*, 1990, **23**, 132–139.

(64) A. Onuki, *Phase Transition Dynamics*, Cambridge University Press, 2004.

(65) P. E. Price and I. H. Romdhane, *AIChE J.*, 2003, **49**, 309–322.

(66) M. Yamamura, T. Kajiwara and H. Kage, *Chemical Engineering Science*, 2003, **58**, 3891–3899.

(67) H. Cook, *Acta Metallurgica*, 1970, **18**, 297–306.

(68) J. W. Cahn, *J. Chem. Phys.*, 1965, **42**, 93.

(69) B. Zhou, *Ph.D. thesis*, Massachusetts Institute of Technology, 2006.

(70) G. I. Töth, M. Zarifi and B. Kvamme, *Phys. Rev. E*, 2016, **93**, 013126.

(71) A. M. Lacasta, J. M. Sancho, A. Hernández-Machado and R. Toral, *Phys. Rev. B*, 1993, **48**, 6854–6857.

(72) I. Lifshitz and V. Slyozov, *Journal of Physics and Chemistry of Solids*, 1961, **19**, 35–50.

(73) C. Wagner, *Zeitschrift für Elektrochemie, Berichte der Bunsengesellschaft für physikalische Chemie*, 1961, **65**, 581–591.

(74) P. W. Voorhees, *J. Stat. Phys*, 1985, **38**, 231–252.

(75) J. Zhu, L.-Q. Chen, J. Shen and V. Tikare, *Phys. Rev. E*, 1999, **60**, 3564–3572.

(76) A. J. Bray and C. L. Emmott, *Physical Review B*, 1995, **52**, R685–R688.

(77) K. Kawasaki and K. Sekimoto, *Macromolecules*, 1989, **22**, 3063–3075.

(78) A. Chakrabarti, R. Toral, J. D. Gunton and M. Muthukumar, *Physical Review Letters*, 1989, **63**, 2072–2075.

(79) M. A. Kotnis and M. Muthukumar, *Macromolecules*, 1992, **25**, 1716–1724.

(80) G. Brown and A. Chakrabarti, *J. Chem. Phys.*, 1993, **98**, 2451.

(81) A. Chakrabarti, R. Toral and J. Gunton, *Phys. Rev. E*, 1993, **47**, 3025–3038.

(82) C. Castellano and S. C. Glotzer, *J. Chem. Phys.*, 1995, **103**, 9363.

(83) A. Aksimentiev, K. Moorthi and R. Holyst, *J. Chem. Phys.*, 2000, **112**, 6049.

(84) E. Siggia, *Phys. Rev. A*, 1979, **20**, 595–605.

(85) A. Bray, *Advances in Physics*, 1994, **43**, 357–459.

(86) G. Tegze, T. Pusztai and L. Gránásy, *Materials Science and Engineering: A*, 2005, **413-414**, 418–422.

(87) M. San Miguel, M. Grant and J. D. Gunton, *Physical Review A*, 1985, **31**, 1001–1005.

(88) H. Chen and A. Chakrabarti, *J. Chem. Phys.*, 1998, **108**, 6006.

(89) R. C. Ball and R. L. H. Essery, *J. Phys.: Condens. Matter*, 1990, **2**, 10303–10320.

(90) R. A. L. Jones, L. J. Norton, E. J. Kramer, F. S. Bates and P. Wiltzius, *Phys. Rev. Lett.*, 1991, **66**, 1326–1329.

(91) K. D. Jandt, J. Heier, F. S. Bates and E. J. Kramer, *Langmuir*, 1996, **12**, 3716–3720.

Supporting information for: "A multi-fluid model for microstructure formation in polymer membranes"

Douglas R. Tree,[†] Kris T. Delaney,[†] Hector D. Ceniceros,[‡] Tatsuhiro Iwama,[¶] and Glenn H. Fredrickson[*,§]

†*Materials Research Laboratory, University of California, Santa Barbara, CA 93106-5121*

‡*Department of Mathematics, University of California, Santa Barbara, CA 93106-5121*

¶*Asahi Kasei Corporation, 2-1 Samejima, Fuji, Shizuoka 416-8501 Japan*

§*Materials Research Laboratory, Materials Department and Chemical Engineering Department, University of California, Santa Barbara, CA 93106-5121*

E-mail: drt@mrl.ucsb.edu

Obtaining Transport Equations from the Rayleighian

In this section, we show how the Rayleighian specified in the main manuscript produces the transport equations in Equations 18–21. Substituting Equations 11, 12 and 17 into Eq. 6 gives the fully specified Rayleighian for the ternary multi-fluid model,

$$R[\{\boldsymbol{v}_i\}] = \int d\boldsymbol{r} \Bigg[\sum_i^{p,n,s} \frac{\zeta_i}{2} \left(\boldsymbol{v}_i - \boldsymbol{v}_m\right)^2 + \frac{1}{2}\, \boldsymbol{\sigma}^{(\mathrm{v})} : \nabla \boldsymbol{v} - p\left(\nabla \cdot \boldsymbol{v}\right) + \sum_i^{p,n} \phi_i \boldsymbol{v}_i \cdot \nabla \mu_i \Bigg]. \tag{1}$$

Component force balances are given by stationary values of the functional derivatives of the Rayleighian (*i.e.*, the Euler-Lagrange equations),

$$\frac{\delta R}{\delta \boldsymbol{v}_i} = \frac{\partial \mathcal{R}}{\partial \boldsymbol{v}_i} - \nabla \cdot \frac{\partial \mathcal{R}}{\partial \nabla \boldsymbol{v}_i} = 0 \tag{2}$$

where $\mathcal{R}$ is the integrand of the Rayleighian. Taking these functional derivatives and substituting Equations 4 and 14 to eliminate $\boldsymbol{v}$ and $\boldsymbol{v}_m$ yields,

$$\frac{\delta R}{\delta \boldsymbol{v}_p} = \frac{\zeta_p \zeta_n}{\zeta}(\boldsymbol{v}_p - \boldsymbol{v}_n) + \frac{\zeta_p \zeta_s}{\zeta}(\boldsymbol{v}_p - \boldsymbol{v}_s) - \phi_p \nabla \cdot \boldsymbol{\sigma}^{(\mathrm{v})} + \phi_p \nabla p + \phi_p \nabla \mu_p \tag{3}$$

$$\frac{\delta R}{\delta \boldsymbol{v}_n} = \frac{\zeta_p \zeta_n}{\zeta}(\boldsymbol{v}_n - \boldsymbol{v}_p) + \frac{\zeta_n \zeta_s}{\zeta}(\boldsymbol{v}_n - \boldsymbol{v}_s) - \phi_n \nabla \cdot \boldsymbol{\sigma}^{(\mathrm{v})} + \phi_n \nabla p + \phi_n \nabla \mu_n \tag{4}$$

$$\frac{\delta R}{\delta \boldsymbol{v}_s} = \frac{\zeta_p \zeta_s}{\zeta}(\boldsymbol{v}_s - \boldsymbol{v}_p) + \frac{\zeta_n \zeta_s}{\zeta}(\boldsymbol{v}_s - \boldsymbol{v}_n) - \phi_s \nabla \cdot \boldsymbol{\sigma}^{(\mathrm{v})} + \phi_s \nabla p. \tag{5}$$

The total momentum equation is readily obtained by summing Equations 3 through 5,

$$0 = -\nabla p + \nabla \cdot \boldsymbol{\sigma}^{(v)} - \sum_i^{p,n} \phi_i \nabla \mu_i. \tag{6}$$

This equation can be more compactly written by introducing the osmotic stress tensor,[S1–S4]

$$\nabla \cdot \boldsymbol{\Pi} = \sum_i^{p,n} \phi_i \nabla \mu_i \tag{7}$$

which gives

$$0 = -\nabla p + \nabla \cdot \boldsymbol{\sigma}^{(v)} - \nabla \cdot \boldsymbol{\Pi}. \tag{8}$$

Component diffusion equations can be obtained by combining Equations 3 through 5 with the conservation of mass expression in Eq. 2. We define the diffusive flux of component i as,

$$\boldsymbol{j}_i = \phi_i \left(\boldsymbol{v} - \boldsymbol{v}_i\right) \tag{9}$$

which allows us to re-write Eq. 2 as,

$$\frac{\partial \phi_i}{\partial t} + \boldsymbol{v} \cdot \nabla \phi_i = \nabla \cdot \boldsymbol{j}_i. \tag{10}$$

Substituting the definition of the friction coefficient from Eq. 15 into Equations 3–5 and using the definition of diffusive flux gives,

$$\boldsymbol{j}_p = \mathrm{v}_0 \zeta_0^{-1} \left[-\phi_p \nabla \cdot \boldsymbol{\sigma}^{(\mathrm{v})} + \phi_p \nabla p + \phi_p \nabla \mu_p \right] \tag{11}$$

$$\boldsymbol{j}_n = \mathrm{v}_0 \zeta_0^{-1} \left[-\phi_n \nabla \cdot \boldsymbol{\sigma}^{(\mathrm{v})} + \phi_n \nabla p + \phi_n \nabla \mu_n \right] \tag{12}$$

$$\boldsymbol{j}_s = -\mathrm{v}_0 \zeta_0^{-1} \left[\phi_s \nabla \cdot \boldsymbol{\sigma}^{(\mathrm{v})} + \phi_s \nabla p \right] \tag{13}$$

To isolate the diffusive flux, we eliminate the pressure terms from Equations 11–13 by performing the operations,

$$\boldsymbol{j}_p(\phi_n + \phi_s) - \phi_p(\boldsymbol{j}_n + \boldsymbol{j}_s) \tag{14}$$

$$\boldsymbol{j}_n(\phi_p + \phi_s) - \phi_n(\boldsymbol{j}_p + \boldsymbol{j}_s) \tag{15}$$

and use the fact that (i) $\sum_i^{p,n,s} \phi_i = 1$ and (ii) $\sum_i^{p,n,s} \boldsymbol{j}_i = 0$. With these manipulations, Eq. 10 becomes,

$$\frac{\partial \phi_p}{\partial t} + \boldsymbol{v} \cdot \nabla \phi_p = \frac{\mathrm{v}_0}{\zeta_0} \nabla \cdot \left[\phi_p(1 - \phi_p) \nabla \mu_p - \phi_p \phi_n \nabla \mu_n \right] \tag{16}$$

$$\frac{\partial \phi_n}{\partial t} + \boldsymbol{v} \cdot \nabla \phi_n = \frac{\mathrm{v}_0}{\zeta_0} \nabla \cdot \left[-\phi_p \phi_n \nabla \mu_p + \phi_n(1 - \phi_n) \nabla \mu_n \right] \tag{17}$$

which are more compactly written matrix notation as

$$\frac{\partial \phi_i}{\partial t} + \boldsymbol{v} \cdot \nabla \phi_i = \nabla \cdot \left(\sum_{j=1}^{p,n} M_{ij} \nabla \mu_j \right) \tag{18}$$

where we have introduced the component mobility matrix

$$M_{pp} = \frac{\mathrm{v}_0}{\zeta_0}\phi_p(1-\phi_p) \tag{19}$$

$$M_{pn} = M_{np} = -\frac{\mathrm{v}_0}{\zeta_0}\phi_p\phi_n \tag{20}$$

$$M_{nn} = \frac{\mathrm{v}_0}{\zeta_0}\phi_n(1-\phi_n). \tag{21}$$

The gradient of the chemical potential appears in both Equations 8 and 18. Taking the requisite functional derivatives per the definition in Eq. 10 yields,

$$\mu_i = \frac{k_B T}{\mathrm{v}_0}\left(\frac{\partial f_0}{\partial \phi_i} - \kappa_i \nabla^2 \phi_i\right) \tag{22}$$

where $\partial f_0/\partial\phi_i$ is the derivative of the homogeneous free energy in Eq. 8 with respect to volume fraction of component i. Taking the gradient and using the chain rule gives a chemical potential gradient with explicit volume fraction terms,

$$\nabla\mu_i = \frac{k_B T}{\mathrm{v}_0}\sum_j^{p,n}\left[H_{ij}\nabla\phi_j - K_{ij}\nabla\nabla^2\phi_j\right] \tag{23}$$

where

$$H_{pp} = (N_p\phi_p)^{-1} + (N_s\phi_s)^{-1} - 2\chi_{ps} \tag{24}$$

$$H_{pn} = H_{np} = (N_s\phi_s)^{-1} + \chi_{pn} - \chi_{ns} - \chi_{ps} \tag{25}$$

$$H_{nn} = (N_n\phi_n)^{-1} + (N_s\phi_s)^{-1} - 2\chi_{ns} \tag{26}$$

is the Hessian matrix, and

$$K_{pp} = \kappa_p \tag{27}$$

$$K_{pn} = K_{np} = 0 \tag{28}$$

Table S1: Characteristic Scales

Scale	Expression	Description
R	$bN_r^{1/2}$	end-to-end distance of the reference polymer
τ	$N_r^2\eta_r \mathrm{v}_0/k_BT$	Rouse time of reference polymer
p^*	η_r/τ	viscous stress scale

$$K_{nn} = \kappa_n \tag{29}$$

is the matrix of gradient coefficients. Substituting Eq. 23 into Equations 8 and 18 gives,

$$-\nabla p + \nabla \cdot \boldsymbol{\sigma}^{(v)} = \frac{k_BT}{\mathrm{v}_0} \sum_{i,j}^{p,n} \phi_i \left(H_{ij} \nabla \phi_j - K_{ij} \nabla \nabla^2 \phi_j \right) \tag{30}$$

$$\frac{\partial \phi_i}{\partial t} + \boldsymbol{v} \cdot \nabla \phi_i = \frac{k_BT}{\mathrm{v}_0} \nabla \cdot \left[\sum_{j,k}^{p,n} M_{ij} \left(H_{jk} \nabla \phi_k - K_{jk} \nabla \nabla^2 \phi_k \right) \right]. \tag{31}$$

With a fully specified model, we seek to write Equations 30 and 31 in dimensionless form. We define the characteristic length scale to be

$$R = bN_r^{1/2} \tag{32}$$

the end-to-end distance of a reference polymer of length N_r. The characteristic time scale is set to the Rouse time in a solution with a reference viscosity η_r,

$$\tau = \frac{N_r^2 \eta_r \mathrm{v}_0}{k_BT} \tag{33}$$

and the characteristic pressure scale is set to be

$$p^* = \eta_r/\tau. \tag{34}$$

These characteristic scales are summarized in Table S1.

Using the definitions of R, τ and p^*, the momentum equation from Eq. 30 becomes,

$$\begin{aligned}-\tilde{\nabla}\tilde{p}+\tilde{\nabla}\cdot\tilde{\boldsymbol{\sigma}}^{(v)} =&\frac{k_BT}{\mathrm{v}_0}\frac{\tau}{\eta_r}\sum_{i,j}^{p,n}\phi_i\left(H_{ij}\tilde{\nabla}\phi_j-K_{ij}R^{-2}\tilde{\nabla}\tilde{\nabla}^2\phi_j\right)\\ =&N_r\sum_{i,j}^{p,n}\phi_i\left[(N_rH_{ij})\tilde{\nabla}\phi_j-(N_rR^{-2}K_{ij})\tilde{\nabla}\tilde{\nabla}^2\phi_j\right]\end{aligned}\tag{35}$$

where $\tilde{\nabla}=\nabla R$, $\tilde{p}=p/p^*$ and $\tilde{\boldsymbol{\sigma}}^{(v)}=\boldsymbol{\sigma}^{(v)}/p^*$. Similarly, the diffusion equation becomes,

$$\begin{aligned}\frac{\partial\phi_i}{\partial\tilde{t}}+\tilde{\boldsymbol{v}}\cdot\tilde{\nabla}\phi_i =&\frac{k_BT}{\mathrm{v}_0}\frac{\tau}{R^2}\tilde{\nabla}\cdot\left[\sum_{j,k}^{p,n}M_{ij}\left(H_{jk}\tilde{\nabla}\phi_k-R^{-2}K_{jk}\tilde{\nabla}\tilde{\nabla}^2\phi_k\right)\right]\\ =&\nabla\cdot\left\{\sum_{j,k}^{p,n}\left(\eta_rb^{-2}M_{ij}\right)\left[\left(N_rH_{jk}\right)\nabla\phi_k-\left(N_rR^{-2}K_{jk}\right)\nabla\nabla^2\phi_k\right]\right\}\end{aligned}\tag{36}$$

where $\tilde{t}=t/\tau$, $\tilde{\boldsymbol{v}}=\boldsymbol{v}\tau/R$. The non-dimensionalization procedure suggests that we define a dimensionless gradient coefficient $\tilde{\kappa}_i=N_rR^{-2}\kappa_i$, a dimensionless mobility matrix $\tilde{M}_{ij}=\eta_rb^{-2}M_{ij}$ and a re-scaled Hessian matrix $\tilde{H}_{ij}=N_rH_{ij}$, which appear in Equations 22–24.

Finally, note that the Peclet number, which would normally appear before the diffusion term in Eq. 36 is equal to unity. This is a consequence of the fact that all of the convective flows in the system are internally generated. If there had been boundary conditions prescribing alternate length and time scales, it would have been possible to obtain $\mathrm{Pe}\neq 1$. However, the capillary number does appear in Eq. 35. Here there are two energy scales; surface energy is characterized by k_BT and viscous energy by η_rR^3/τ. This means that the capillary number

$$\mathrm{Ca}=N_r^{-1}\tag{37}$$

is fixed by the reference degree of polymerization and is a consequence of the way that the surface forces and viscous forces scale with the reference length scale. At the monomer length scale, $N_r=N_s\approx 1$ and $\mathrm{Ca}\approx 1$. However, zooming out to the scale of the polymer radius of gyration, $N_r=N_p$, $\mathrm{Ca}=N_p^{-1}$ and the surface tension forces are much stronger.

Ternary Phase Diagram

For fixed N_i and χ_{ij}, the homogeneous free energy in Eq. 8 can be used to produce a ternary phase diagram consisting of (i) a binodal, (ii) a spinodal and (iii) a critical point.

The binodal curve is typically obtained by equating the chemical potentials of each species in both phases. Because f_0 is an intrinsic quantity, it is convenient to use an equivalent formalism where we equate the exchange chemical potentials

$$\mu_i = \frac{\partial f_0}{\partial \phi_i} \tag{38}$$

and the osmotic pressure

$$\Pi = f_0 - \sum_i \phi_i \mu_i \tag{39}$$

in each phase.[S5] Substituting Eq. 8 into Equations 38 and 39 and assuming pseudo-binary parameters, gives

$$\frac{1}{N}\ln\left(\frac{\phi_p^\alpha}{\phi_p^\beta}\right) - \ln\left(\frac{1-\phi_p^\alpha-\phi_n^\alpha}{1-\phi_p^\beta-\phi_n^\beta}\right) + \chi\left(\phi_n^\alpha - \phi_n^\beta\right) = 0 \tag{40}$$

$$\ln\left(\frac{\phi_n^\alpha}{\phi_n^\beta}\right) - \ln\left(\frac{1-\phi_p^\alpha-\phi_n^\alpha}{1-\phi_p^\beta-\phi_n^\beta}\right) + \chi\left(\phi_p^\alpha - \phi_p^\beta\right) = 0 \tag{41}$$

$$\ln\left(\frac{1-\phi_p^\alpha-\phi_n^\alpha}{1-\phi_p^\beta-\phi_n^\beta}\right) + \left(\phi_p^\alpha - \phi_p^\beta\right)\left(1-\frac{1}{N}\right) - \chi\left(\phi_p^\alpha\phi_n^\alpha - \phi_p^\beta\phi_n^\beta\right) = 0 \tag{42}$$

With four unknowns (ϕ_p^α, ϕ_n^α, ϕ_p^β, ϕ_n^β), these three equations define the binodal curve in composition space for a given χ and N.

The spinodal is calculated by setting the determinant of the Hessian matrix in Eq. 23 to zero,

$$Z \equiv \begin{vmatrix} H_{pp} & H_{nn} \\ H_{pn} & H_{np} \end{vmatrix} = 0 \tag{43}$$

and the critical point is given when both Eq. 43 and

$$\begin{vmatrix} \dfrac{\partial Z}{\partial \phi_p} & H_{nn} \\ \dfrac{\partial Z}{\partial \phi_n} & H_{np} \end{vmatrix} = 0 \tag{44}$$

are satisfied.[S6–S8] Both equations are straightforward to generate, but too long to conveniently reproduce here.

Without further approximation, the solution to all three equations require numerical methods. For this paper, we compute the phase diagram using a custom code in Python. We find the critical point by simultaneously solving Equations 43 and 44. We then solve Eq. 43 from $\phi_s = 0$ to the critical point, resolving the two branches of the spinodal. Finally, we compute the two branches of the binodals by first computing the phase co-existence point for a binary system ($\phi_s = 0$), and then solve Eq. 40- 42 marching ϕ_p^α from the polymer-rich solution of the binary problem to the critical point. Unlike Yilmaz and McHugh,[S7] we did not need to resort to a least-squares method to avoid the trivial solution. Rather, we used scipy's `optimize.fsolve()` function with an analytical Jacobian and a first-order continuation method to obtain initial guesses.

Theory of a 1D interface

The concentration profiles for our model can be found by minimizing the interfacial free energy,

$$\gamma[\phi_p, \phi_n] = F[\phi_p, \phi_n] - \frac{k_B T}{V} \int d\boldsymbol{r}\, f_{eq}(\phi_p, \phi_n) \tag{45}$$

of a two phase system where the α-phase $\{\phi_p^\alpha, \phi_n^\alpha\}$ at the left boundary, $x = -\infty$, is in equilibrium with the β-phase $\{\phi_p^\beta, \phi_n^\beta\}$ at the right boundary, $x = \infty$. $F[\phi_p, \phi_n]$ is the free

energy functional given in Eq. 7 and

$$f_{eq}(\phi_p, \phi_n) = f_0(\phi_p^\alpha, \phi_n^\alpha) + (\phi_p - \phi_p^\alpha)\mu_p(\phi_p^\alpha, \phi_n^\alpha) + (\phi_n - \phi_n^\alpha)\mu_n(\phi_p^\alpha, \phi_n^\alpha) \tag{46}$$

is the equilibrium free energy absent any interfaces. Note that the choice of the α-phase for Eq. 46 is arbitrary and the μ_i that appear are the exchange chemical potentials.

There are two barriers to obtaining analytical results for the interfacial profiles described by Eq. 45. The first is that $\gamma[\phi_p, \phi_n]$ describes the profiles of both $\phi_p(\boldsymbol{r})$ and $\phi_n(\boldsymbol{r})$, requiring a simultaneous solution to two Euler-Lagrange equations. To avoid this, we assume that the solvent concentration is constant, $\phi_s \approx \bar{\phi}_s$, making the model truly binary ($\phi = \phi_p$, $\phi_n = 1 - \phi - \bar{\phi}_s$). In general, the solvent concentration is not truly constant between both phases, since the solvent may partition unequally as well as concentrate at the polymer/non-solvent interface. However, this effect is small enough to neglect in the strong segregation limit, which we justify below.

Assuming a binary system, and using the notation for the pseudo-binary parameters given above, we re-write Eq. 45 for a 1D interface as,

$$\gamma[\phi] = \frac{k_B T}{b^2} \int \frac{dx}{b} \left[\Delta f(\phi) + K(\dot{\phi}) \right] \tag{47}$$

where

$$\Delta f(\phi) = f_0(\phi) - f_0(\phi^\alpha) - (\phi - \phi^\alpha)\mu(\phi^\alpha) \tag{48}$$

$$K(\dot{\phi}) = \kappa\, \dot{\phi}^2 \tag{49}$$

and

$$f_0(\phi) = \frac{\phi}{N} \ln \phi + \left(1 - \phi - \bar{\phi}_s\right) \ln \left(1 - \phi - \bar{\phi}_s\right) + \bar{\phi}_s \ln \bar{\phi}_s + \chi \phi \left(1 - \phi - \bar{\phi}_s\right) \tag{50}$$

with $\mu = \partial f_0/\partial\phi$. Eq. 47 has a Lagrangian form, which immediately implies that

$$\dot{\phi}(x) = \left[\frac{\Delta f(\phi)}{\kappa}\right]^{1/2} \tag{51}$$

The second barrier to progress is the appearance of logarithmic terms in Eq. 50. To surmount this barrier, we assume that the phases are strongly segregated ($\chi \gg 1$ and $N \gg 1$) and use perturbation theory.[S5] Expanding $f_0(\phi)$ in this limit allows us to find the equilibrium concentrations, ϕ_α and ϕ_β. Equating exchange chemical potentials, $\mu_\alpha = \mu_\beta$, and osmotic pressures, $\Pi_\alpha = \Pi_\beta$, for the pseudo-binary model in both phases gives,

$$\frac{1}{\chi N}\ln\left(\frac{\varphi^\alpha}{\varphi^\beta}\right) - \frac{1}{\chi}\ln\left(\frac{1-\varphi^\alpha}{1-\varphi^\beta}\right) - 2\left(1-\bar{\phi}_s\right)\left(\varphi^\alpha - \varphi^\beta\right) = 0 \tag{52}$$

$$\frac{1}{\chi}\ln\left(\frac{1-\varphi^\alpha}{1-\varphi^\beta}\right) + \left(\varphi^\alpha - \varphi^\beta\right)\left(\frac{1}{\chi} - \frac{1}{\chi N}\right) + \left(1-\bar{\phi}_s\right)\left[(\varphi^\alpha)^2 - (\varphi^\beta)^2\right] = 0 \tag{53}$$

where we have introduced the reduced volume fraction

$$\varphi^\nu = \phi^\nu / \left(1-\bar{\phi}_s\right) \tag{54}$$

such that $\varphi \in [0,1]$ for $\nu \in [\alpha,\beta]$.

Assuming that $\varphi^\alpha \approx \epsilon^\alpha$ and $\varphi^\beta \approx 1-\epsilon^\beta$, Eq. 52 and Eq. 53 reduce to,

$$\frac{1}{\chi N}\left(\ln\epsilon^\alpha + \epsilon^\beta\right) + \frac{1}{\chi}\left(\epsilon^\alpha + \ln\epsilon^\beta\right) - 2\left(1-\bar{\phi}_s\right)\left(\epsilon^\alpha + \epsilon^\beta - 1\right) = 0 \tag{55}$$

$$-\frac{1}{\chi}\left(\epsilon^\alpha + \ln\epsilon^\beta\right) + \left(\epsilon^\alpha + \epsilon^\beta - 1\right)\left(\frac{1}{\chi} - \frac{1}{\chi N}\right) + \left(1-\bar{\phi}_s\right)\left[(\epsilon^\alpha)^2 - (1-\epsilon^\beta)^2\right] = 0 \tag{56}$$

where we have used the Taylor expansion $\ln(1-\epsilon) \approx -\epsilon$ when appropriate. The largest term in Eq. 55–56 are of $\mathrm{O}(\ln\epsilon)$, so we can neglect terms of $\mathrm{O}(\epsilon)$. Doing so and re-arranging

gives,

$$\epsilon^{\alpha} = \exp\left[-\chi N(1-\bar{\phi}_s)\right] \tag{57}$$

$$\epsilon^{\beta} = \exp\left[-\chi(1-\bar{\phi}_s)\right] \tag{58}$$

to leading order when $\chi \gg 1$ and $N \gg 1$. It can be shown using a similar perturbation expansion of the phase equilibrium equations for the full ternary model, that the solvent concentration is constant at $\mathrm{O}(\ln \epsilon)$, justifying the pseudo-binary assumption.

Fully solving Eq. 51 for the interfacial profile requires numerical methods, but, we can obtain an expression for the interfacial width regardless. A characteristic interfacial width can be defined as,[S5,S9]

$$l = \frac{\phi^{\beta} - \phi^{\alpha}}{\dot{\phi}(x=0)} \tag{59}$$

where we can substitute the right hand side of Eq. 51 for $\dot{\phi}$. Doing so requires an expression for Δf_0, which can be obtained by combining Eq. 48 and Eq. 50,

$$\Delta f_0(\phi) = \frac{\phi}{N}\ln\left(\frac{\phi}{\phi^{\alpha}}\right) + (1-\phi-\bar{\phi}_s)\ln\left(\frac{1-\phi-\bar{\phi}_s}{1-\phi^{\alpha}-\bar{\phi}_s}\right) + \left(1-\frac{1}{N}\right)(\phi-\phi^{\alpha}) - \chi\left(\phi-\phi^{\alpha}\right)^2 \tag{60}$$

Assuming that $\varphi = 1/2$ at $x = 0$, and using the binodal curves described by Equations 57 and 58 gives the width in Eq. 52, where terms smaller than $\mathrm{O}(\frac{1}{\chi})$ and $\mathrm{O}(\frac{1}{\chi N})$ have been neglected.

Linear Stability Analysis

We begin by neglecting hydrodynamics (set $\boldsymbol{v} = 0$ everywhere) and linearizing Eq. 18 about the homogeneous state $\{\bar{\phi}_p, \bar{\phi}_n\}$,

$$\frac{\partial}{\partial t}\delta\phi_i = \sum_{j,k} \bar{M}_{ij} \left(\bar{H}_{jk}\nabla^2\delta\phi_k - K_{jk}\nabla^4\delta\phi_k\right) \tag{61}$$

where $\delta\phi_i = \phi_i - \bar{\phi}_i$, and $\bar{M}_{ij}$ and $\bar{H}_{jk}$ indicate constant matrices evaluated at $\bar{\phi}_p$ and $\bar{\phi}_n$. Taking the Fourier transform gives,

$$\frac{\partial}{\partial t}\delta\hat{\phi}_i = \sum_{j,k} \left(-\bar{M}_{ij}\bar{H}_{jk}\, q^2 - \bar{M}_{ij}K_{jk}\, q^4\right) \delta\hat{\phi}_k \tag{62}$$

which is useful, since the derivative operators can be simply expressed in Fourier space. Eq. 62 is a system of linear, first order differential equations, which has a formal solution in Fourier-space of

$$\delta\hat{\phi}_i(q,t) = \sum_k \exp\left[A_{ik}(q)t\right] \delta\hat{\phi}_k(q,0) \tag{63}$$

where

$$A_{ik}(q) = -\sum_j \left(\bar{M}_{ij}\bar{H}_{jk}\, q^2 + \bar{M}_{ij}K_{jk}\, q^4\right) \tag{64}$$

From Eq. 63 it is clear that $\hat{\phi}(q,t)$ becomes unstable (thus precipitating spinodal decomposition) when $A_{ik}(q)$ is no longer negative definite. By definition, $A_{ik}(q)$ is non-negative definite when one eigenvalue is greater than or equal to zero for some value of q. This can be made explicit by using a similarity transform of A_{ik}, giving

$$\delta\hat{\phi}_i(q,t) = \sum_{j,k,l} X_{ij} \exp\left[\Lambda_{jk}t\right] X^{-1}_{kl}\delta\hat{\phi}_l(q,0) \tag{65}$$

where

$$\Lambda_{jk} = \begin{pmatrix} \lambda_+ & 0 \\ 0 & \lambda_- \end{pmatrix} \tag{66}$$

and X_{ij} are the eigenvalue and eigenvector matrices of $A_{ik}(q)$. Since $A_{ik}(q)$ is rank two, there is a simple formula for the eigenvalues

$$\lambda_\pm = \frac{\mathcal{T}}{2} \pm \frac{(\mathcal{T}^2 - 4\mathcal{D})^{1/2}}{2} \tag{67}$$

where $\mathcal{T} = \mathrm{tr}[A_{ik}(q)]$ and $\mathcal{D} = \det[A_{ik}(q)]$. By inspection, $\mathcal{T}$ is always less than zero. Therefore, λ_+ can only be positive when $\mathcal{D} < 0$, making $\mathcal{D} = 0$ the stability criteria.

We can decompose this determinant into two terms: one that depends on the mobility and one that depends on the equilibrium parameters alone,

$$\det[A_{ik}(q)] = -\det(\bar{M}_{ij} q^2)\ \det(\bar{H}_{jk} + K_{jk}\, q^2) \tag{68}$$

It can be shown (and it is also physically intuitive) that the mobility matrix, $\bar{M}_{ij}$, is always positive definite, and therefore it is only necessary to consider

$$\det(\bar{H}_{jk} + K_{jk}\, q^2) = 0 \tag{69}$$

for the stability analysis. This is re-assuring, since kinetics should not determine thermodynamic stability.

Re-writing Eq. 69,

$$\begin{vmatrix} \bar{H}_{pp} + \kappa_p q^2 & \bar{H}_{pn} \\ \bar{H}_{np} & \bar{H}_{nn} + \kappa_p q^2 \end{vmatrix} = 0 \tag{70}$$

highlights its relationship with Eq. 43, proving that the preceding analysis generates the spinodal curve when κ_p and κ_n are zero. When κ_p and κ_n are non-zero, a finite size system is stabilized by the gradient free energy until a critical wavelength, $2\pi/q_c$, above which the

system becomes unstable. The critical wavenumber is given by solving Eq. 70, which is a bi-quadratic equation in q. Using the quadratic equation yields,

$$q_c^2 = -\left(\frac{\bar{H}_{pp}}{2\kappa_p} + \frac{\bar{H}_{nn}}{2\kappa_n}\right) \pm \left[\left(\frac{\bar{H}_{pp}}{2\kappa_p} - \frac{\bar{H}_{nn}}{2\kappa_n}\right)^2 + 4\frac{\bar{H}_{pn}}{2\kappa_p}\frac{\bar{H}_{np}}{2\kappa_n}\right]^{1/2}. \tag{71}$$

Once unstable, the spinodal decomposition is dominated by the fastest growing mode, q_m, which is the mode that maximizes $\lambda_+(q)$. Using its definition in Eq. 67 and the definition of the diffusivity matrix (D_{ij}) and the gradient matrix (B_{ij}) in Equations 56 and 28, we can get an expression for λ_+ in terms of D_{ij} and B_{ij},

$$\begin{aligned}\lambda_+ = &-\frac{q^2}{2}\left[(D_{pp} + D_{nn}) + (B_{pp} + B_{nn})q^2\right] &(72)\\ &+ q^2\Big[\left\{(D_{pp} - D_{nn}) + (B_{pp} - B_{nn})q^2\right\}^2 &(73)\\ &+ 4(D_{pn} + B_{pn}q^2)(D_{np} + B_{np}q^2)\Big]^{1/2} &(74)\end{aligned}$$

The fastest growing mode can be found by solving

$$\left.\frac{d\lambda_+}{dq}\right|_{q=q_m} = 0 \tag{75}$$

Unfortunately, there is no convenient closed-form expression for q_m for general parameters, like there is for q_c. However, Eq. 75 can be re-written in a more convenient form for numerical root-finding

$$\lambda_+\frac{d\mathcal{T}}{dq} - \frac{d\mathcal{D}}{dq} = 0 \tag{76}$$

which is valid so long as $\mathcal{T}^2 \neq 4\mathcal{D}$. Additionally, if we assume that the mobility and gradient matrices are scalars ($M_{ij} = M\delta_{ij}$ and $K_{ij} = \kappa\delta_{ij}$), then Eq. 72 is greatly simplified. In this case the fastest growing mode becomes,

$$q_m^2 = \frac{q_c^2}{2} \tag{77}$$

which is equivalent to the relation between q_m and q_c for binary systems.[S10]

Finally, note that in addition to q_m, one also obtains the rate of spinodal decomposition from the preceding analysis. The rate is given by

$$\lambda_m \equiv \lambda_+(q_m) \tag{78}$$

and has units of inverse time. For the case of scalar mobility and gradient matrices, one obtains the simple expression

$$\lambda_m = M\kappa q_m^4 \tag{79}$$

Dynamic scaling

To ensure that the coarsening exponent is not a simulation artifact, we verify in Figure S1 that the polymer structure factor, $S(q)$, and polymer density correlation function, $g(r)$, obey dynamic scaling at long times. Dynamic scaling requires the system to be self-similar, and therefore the structure factor and the density correlation function should both collapse to universal curves when scaled by some characteristic length, L. The structure factor has units of length squared and the correlation function is dimensionless, so $L^{-2}S(Lq)$ and $g(r/L)$ should be universal at long times.

Figure S1(a) shows that the structure factor for $\{\phi_p, \phi_n\} = \{0.3, 0.65\}$ (blue circles in Figures 6 and 7) scaled by $\langle q^{-1} \rangle$ for $t \geq 4096$ collapses to a universal curve. Figure S1(b) shows a similar collapse for the real-space correlation function, $g(r/R_g)$ where R_g is the location of the first zero of the unscaled $g(r)$. The inset to Figure S1(b) shows the product of R_g and $\langle q \rangle$, which approaches a steady value as $t \to \infty$. The latter plot demonstrates that because the system is self-similar, either $\langle q \rangle$ or R_g can be used as a characteristic length.

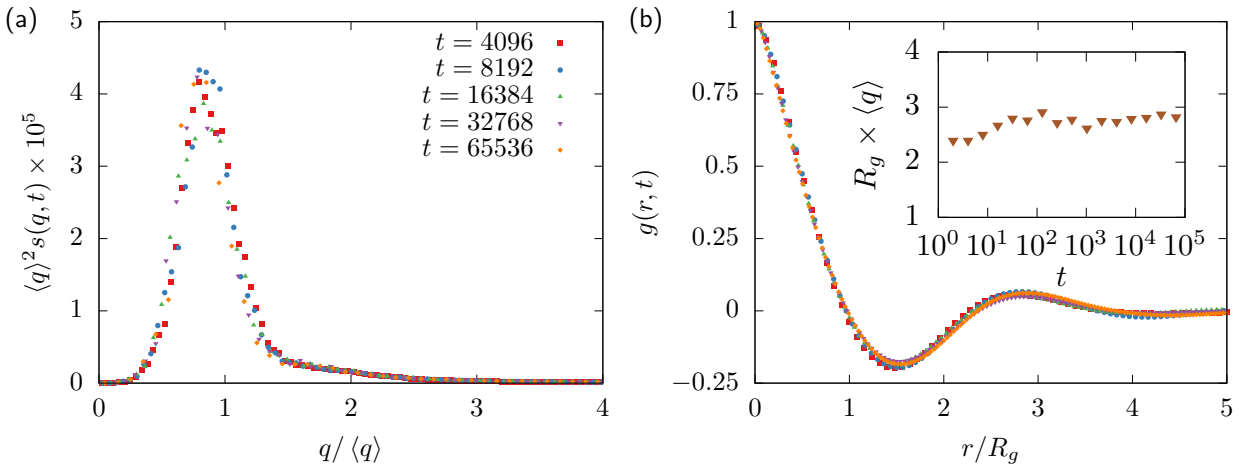

Figure S1: (a) Polymer structure factor versus wavevector, scaled by the first moment $\langle q \rangle$. (b) Polymer density correlation function versus radial distance, r, scaled by R_g, the first zero of $g(r)$. (inset to b) Product of R_g and $\langle q \rangle$ as a function of time, showing the equivalence of each measure of the domain size to within a constant value at long times. Data are from the one of the sets presented in Figures 6 and 7 (closed blue circles, diffusion only) with parameters: $N = 20$, $\chi = 0.973, \kappa = 2, \{\phi_p, \phi_n\} = \{0.3, 0.65\}$.

References

(S1) M. Doi and A. Onuki, *J. Phys. II France*, 1992, **2**, 1631–1656.

(S2) M. Cromer, M. C. Villet, G. H. Fredrickson, L. Gary Leal, R. Stepanyan and M. J. H. Bulters, *J. Rheol.*, 2013, **57**, 1211–1235.

(S3) S. T. Milner, *Phys. Rev. E*, 1993, **48**, 3674–3691.

(S4) H. Tanaka, *J. Phys.-Condens. Mat.*, 2000, **12**, R207.

(S5) D. Broseta, G. H. Fredrickson, E. Helfand and L. Leibler, *Macromolecules*, 1990, **23**, 132–139.

(S6) D. Broseta and G. H. Fredrickson, *J. Chem. Phys.*, 1990, **93**, 2927.

(S7) L. Yilmaz and A. J. McHugh, *J. Appl. Polym. Sci.*, 1986, **31**, 997–1018.

(S8) J. W. Gibbs, in *The Scientific Papers of J. Willard Gibbs. Vol 1. Thermodynamics*, Longmans, Green and Co., 1906, ch. On the Equilibrium of Heterogeneous Substances.

(S9) J. W. Cahn and J. E. Hilliard, *J. Chem. Phys.*, 1958, **28**, 258–267.

(S10) J. W. Cahn, *J. Chem. Phys.*, 1965, **42**, 93.